

1 **Measurement report: Insights into the high temporal variability of**  
2 **atmospheric carbon dioxide (CO<sub>2</sub>) at a suburban station in the Indo-**  
3 **Gangetic Plain**

4  
5 Vimal Jose Vazhathara<sup>1, \*</sup>, Ravi Kumar Kunchala<sup>1</sup>, Sajeev Philip<sup>1</sup>, Jaswant Rathore<sup>1</sup>, Dilip  
6 Ganguly<sup>1</sup>, Sagnik Dey<sup>1,2</sup>, Tomoki Nakayama<sup>3</sup>, Yutaka Matsumi<sup>4,5</sup> and Prabir K. Patra<sup>4,6</sup>

7  
8 <sup>1</sup>Centre for Atmospheric Sciences, Indian Institute of Technology Delhi, New Delhi, India.

9 <sup>2</sup>Centre of Excellence for Research on Clean Air, Indian Institute of Technology Delhi, New  
10 Delhi, India

11 <sup>3</sup>Graduate School of Integrated Science and Technology, Nagasaki University, 1–14 Bunkyo-  
12 machi, Nagasaki, Nagasaki, 852–8521, Japan

13 <sup>4</sup>Research Institute for Humanity and Nature, Kyoto, Japan

14 <sup>5</sup>Institute for Space-Earth Environmental Research, Nagoya University, Nagoya, Japan

15 <sup>6</sup>Japan Agency for Marine-Earth Science and Technology (JAMSTEC), Yokohama, Japan.

16 \*Correspondence to: Vimal Jose Vazhathara (vimaljosevazhathara@gmail.com), Centre for  
17 Atmospheric Sciences, Indian Institute of Technology Delhi, New Delhi, 110016, India

18

19 **Abstract**

20 The unusual weather patterns and large anthropogenic emissions over the Indo-Gangetic Plain  
21 (IGP) make it a significant hotspot of greenhouse gases like carbon dioxide (CO<sub>2</sub>). Given the  
22 significance of the IGP and highly populated Delhi National Capital Region (Delhi-NCR), a  
23 GHG observatory was established at a suburban monitoring station in Sonipat, Haryana  
24 (28.95°N, 77.10°E; 228m asl), about 45 km north of the Delhi state boundary. Using a laser-  
25 based cavity ring-down spectroscopy (CRDS) technique, we measured CO<sub>2</sub> mole fraction from  
26 February 2023 to January 2025. An annual average CO<sub>2</sub> mole fraction of 440.8±19.7 parts per  
27 million (ppm) was recorded in 2024, which includes a strong seasonal variability, ranging from

28 422.6±23.3 ppm during the monsoon (June- September) to 456.4±30.8 ppm in post-monsoon  
29 (October -November). A strong CO<sub>2</sub> diurnal amplitude of 29 ppm in May and 63 ppm in  
30 October was observed mainly due to seasonal changes in boundary layer mixing (faster in May  
31 than October) and biospheric activity (weaker in May than October). Further investigation of  
32 the drivers of strong seasonal and diurnal CO<sub>2</sub> variability over IGP revealed a strong contrast  
33 to other global monitoring stations in the same latitude band. A strong correlation between CO<sub>2</sub>  
34 and methane (CH<sub>4</sub>) indicated a co-located emission source, while the strong positive correlation  
35 between CO<sub>2</sub> and carbon monoxide (CO) during post-monsoon emerges due to emissions from  
36 biomass burning. We demonstrated that the high temporal CO<sub>2</sub> variability in the IGP region is  
37 driven by the complex interplay of local anthropogenic and biomass burning emissions,  
38 biospheric fluxes, and prevailing meteorology.

39

## 40 **1. Introduction**

41 Carbon dioxide (CO<sub>2</sub>) is the major greenhouse gas (GHG) contributing to climate change and  
42 global warming ( IPCC, 2021; Fawzy et al., 2020). Due to the long lifetime and high radiative  
43 forcing potential, CO<sub>2</sub> can have a significant impact on global and regional climate (Wang et  
44 al., 2010). The atmospheric CO<sub>2</sub> mole fraction has increased from 278 parts per million (ppm)  
45 in the pre-industrial period to 427 ppm in 2025 (NOAA, <https://gml.noaa.gov>; Wigley (1983).  
46 This rapid increase in the atmospheric fraction of CO<sub>2</sub> is primarily due to the combustion of  
47 fossil fuels, cement manufacture, deforestation, and other industrial processes ( Stocker et al.,  
48 2013; Huang et al., 2016; Yoro and Daramola, 2020). A comprehensive understanding of the  
49 sources and sinks of CO<sub>2</sub> is critical for developing national policies to mitigate climate change  
50 impacts.

51 India is the third-highest CO<sub>2</sub>-emitting nation (8% of total global CO<sub>2</sub>) in the last  
52 decade, as reported by the Global Carbon Project (GCP) (Friedlingstein et al., 2025; Le Quéré  
53 et al., 2018). In particular, the Indo-Gangetic Plain (IGP) region is one of the hotspots of  
54 atmospheric CO<sub>2</sub> mole fraction, primarily due to large fossil fuel emissions and adverse  
55 meteorology (Halder et al., 2021; Krishnapriya et al., 2025; Kuttippurath et al., 2022). Over the  
56 past few decades, the IGP region has witnessed rapid urbanisation, industrialisation, and  
57 agricultural intensification, leading to significant changes in land-use patterns and GHG  
58 emissions (Yoro and Daramola, 2020). Mitigation of anthropogenic CO<sub>2</sub> emissions in the  
59 highly populated IGP region is crucial to reducing the build-up of atmospheric CO<sub>2</sub> mole

60 fractions. Gaining a better understanding of the magnitude of CO<sub>2</sub> sources and sinks and the  
61 local drivers of CO<sub>2</sub> temporal variability over the IGP region is therefore important.

62

63 Continuous monitoring of ground-based CO<sub>2</sub> is of utmost importance for inverse  
64 modelling approaches to understand local-to-regional-scale sources and sinks of CO<sub>2</sub>.  
65 Although GHG mole fractions have been monitored worldwide for decades, GHG monitoring  
66 stations in India are limited (Kunchala et al., 2025; Chakraborty et al., 2020; Kumar et al.,  
67 2021; Patra et al., 2013; Tiwari et al., 2013). The Cape Rama (15.08° N, 73.83° E) station,  
68 situated on India's southwest coast, was the first Indian monitoring station to track CO<sub>2</sub> mole  
69 fraction from 1993 to 2002 (Bhattacharya et al., 2009; Patra et al., 2011; Rayner et al., 2008).  
70 Recently, several monitoring stations have been established over different parts of India to  
71 measure the GHGs (Chandra et al., 2016; Jain et al., 2021; Mahesh et al., 2015; Metya et al.,  
72 2021; Nomura et al., 2021; Pathakoti et al., 2023; Sreenivas et al., 2016; Thilakan et al., 2023;  
73 Tiwari et al., 2014). Studies have also been conducted using aircraft-based measurements  
74 (Niwa et al., 2012; Patra et al., 2011; Schuck et al., 2012; Zhang et al., 2007) and satellite data  
75 products (Das et al., 2023; Kunchala et al., 2022; Nalini et al., 2019; Philip et al., 2022; Xiong  
76 et al., 2009). The incorporation of regional in situ and aircraft-based measurements, along with  
77 satellite columnar CO<sub>2</sub> retrievals, reduced uncertainties in top-down CO<sub>2</sub> flux estimates (Huang  
78 et al., 2008; Niwa et al., 2012; Zhang et al., 2014).

79 To comprehensively understand temporal CO<sub>2</sub> variability and its drivers in the western  
80 IGP region, we have conducted atmospheric CO<sub>2</sub> mole fraction measurements at Sonipat, a  
81 suburban station in the IGP region upwind of Delhi. The continuous measurements from  
82 February 2023 to January 2025 were conducted using laser-based cavity ring-down  
83 spectroscopy. Here, we investigate the novel characteristics of the seasonal and diurnal  
84 variability of atmospheric CO<sub>2</sub> mole fraction at Sonipat. We then identify the key drivers of  
85 the observed temporal CO<sub>2</sub> variability in the region.

86

## 87 **2. Materials and methods**

### 88 **2.1 Monitoring station**

89 The measurements in this study were carried out at the Indian Institute of Technology Delhi  
90 (IIT Delhi) Centre for Atmospheric Sciences (CAS) - Atmospheric Observatory situated at  
91 Sonipat campus (28.95°N, 77.10°E, 228m asl). Sonipat is an upwind suburban region of the  
92 Delhi-NCR, situated in the northern Indian state of Haryana, approximately 45 kilometres north  
93 of Delhi. The monitoring station is surrounded by agricultural fields, a National Highway, and

94 academic institutions (Rathore et al., 2025). Figure 1 shows the location map of the monitoring  
95 station. The climatic conditions over this site are similar to Delhi which has sweltering  
96 summers (March-May), damp or moist monsoons (June - September), and extreme winters.  
97 Similar to Delhi, this region also has frequent haze and smog with low visibility during winter  
98 (December - February) and post-monsoon (October - November) seasons. During the post-  
99 monsoon season, Sonipat experiences large transport of pollutants from the North-West  
100 direction. In addition to the pollutant transport, several local emission sources exist in the  
101 region, such as small industries, vehicular sources, and local biomass burning affecting short-  
102 lived air pollutants (Rathore et al., 2025).

103

## 104 **2.2 Local measurements**

### 105 **2.2.1 GHG measurements**

106 This study utilised the PICARRO G2301 GHG analyser to measure major atmospheric GHG  
107 mole fractions. The PICARRO analyser employs the Cavity Ring-Down Spectroscopy (CRDS)  
108 technique at 0.5 Hz to measure CO<sub>2</sub> mole fraction. The CRDS technique utilises the ring-down  
109 time of light intensity within the cavity to determine the mole fraction of CO<sub>2</sub>, a method  
110 fundamentally different from other measurement techniques such as Non-dispersive Infrared  
111 Spectroscopy (NDIR) and Fourier Transform Infrared Spectroscopy (FTIR). The long sample  
112 interaction path length (approximately 20 km) is a characteristic of CRDS, which enhances  
113 sensitivity compared to conventional techniques based on light-intensity absorption. The cavity  
114 pressure operates at a very low pressure of 140 Torr. This isolates a single spectral feature with  
115 a resolution of 0.0003 cm<sup>-1</sup>, ensuring a linear relationship between peak height or area and mole  
116 fraction. The CRDS provides precise, highly sensitive measurements of gases in ambient air  
117 with a temporal resolution of 5 seconds. The technique has been well validated for measuring  
118 atmospheric CO, CO<sub>2</sub>, and CH<sub>4</sub> mole fractions globally and at some Indian monitoring stations  
119 (Chandra et al., 2016; Chen et al., 2013; Jain et al., 2021).

120 The standard cavity temperature of 45°C (throughout the measurement period) ensures  
121 the necessary etalon mechanical stability of the measurement cavity. The sample air was taken  
122 from the top of the building and above the tree canopy (5 meters above the instrument housing)  
123 through a Teflon (PTFE) tube with an inner diameter of 3 mm using an external vacuum pump  
124 with ~400 SCCM flow rate (residence time ~5.9 s). The air intake height is about 248 m.

125 The Sonipat station, lying on the upwind side of Delhi, is a suburban station with  
126 relatively cleaner air compared to the urban city centre. However, Sonipat cannot be considered  
127 a pristine site due to the impact of local emissions from nearby industries and national

128 highways. We adopted (1) the fifth percentile of the daily data to characterise background mole  
129 fraction at the site (Ammoura et al., 2014; Chandra et al., 2016; Jain et al., 2021), and (2) the  
130 adaptive diurnal minimum variation selection (ADVS) method that considers the diurnal  
131 minimum value as the daily background value (Apadula et al., 2019; Yuan et al., 2018). In this  
132 study, the comparison between the fifth percentile and the ADVS methods showed similar CO<sub>2</sub>  
133 background values (see Fig. S1), and the ADVS method was used for further analysis. The  
134 excess CO<sub>2</sub> mole fractions were then estimated by subtracting the hourly averaged values of  
135 CO<sub>2</sub> from the background mole fraction.

136 The measurements of the atmospheric CH<sub>4</sub> mole fraction were also conducted with the  
137 PICARRO G2301 GHG analyser. The GHG analyser employs the CRDS at 0.5 Hz to measure  
138 CH<sub>4</sub> mole fraction. The mole fractions of CH<sub>4</sub> were determined using the ring-down time of  
139 light intensity, similar to CO<sub>2</sub> mole fractions. Calibration was performed following the  
140 guidelines of the National Oceanic and Atmospheric Administration Earth System Research  
141 Laboratories (NOAA-ESRL, 2020) and the Integrated Carbon Observation System (ICOS)  
142 protocol (Laurent, 2020), using NOAA standard calibration cylinders. Further details of the  
143 calibration process are provided in Supplementary Section S1.

144

### 145 **2.2.2 Trace gas measurements**

146 In addition to the measurements of CO<sub>2</sub> and CH<sub>4</sub>, we also utilised the measurements of trace  
147 gases to establish the species interrelationships and to identify drivers of GHG sources. We  
148 used a compact air-quality measurement instrument with gas sensors (CUPI-G) to continuously  
149 measure air pollutants, including fine particulate matter (PM<sub>2.5</sub>), nitric oxide (NO), nitrogen  
150 dioxide (NO<sub>2</sub>), and carbon monoxide (CO). The sensors used in CUPI-G are a palm-sized  
151 optical PM<sub>2.5</sub> sensor developed by Panasonic, a CO-B4 Carbon Monoxide Sensor, and an NO-  
152 B4 Nitric Oxide Sensor developed by Alphasense. The sensitivity of the PM<sub>2.5</sub> and CO sensors  
153 was evaluated in Nagasaki, Japan, through intercomparisons with reference-grade instruments  
154 employing a beta attenuation monitor (BAM) for PM<sub>2.5</sub> and non-dispersive infrared (NDIR)  
155 spectroscopy for CO measurements (Figure S1). The estimated unit-to-unit variability was 29%  
156 for PM<sub>2.5</sub> sensors and 21% for CO sensors. Further details on the sensor specifications and the  
157 calibration methodology are described in Mangaraj et al. (2025).

158

### 159 **2.2.3 Local meteorology measurements**

160 A Vaisala Ceilometer lidar CL61 provides real-time measurements of cloud base height (CBH)  
161 for up to five layers, along with depolarisation measurements, under all weather conditions. To

162 determine the Planetary boundary layer height (PBLH) from the range-corrected attenuated  
163 backscatter data, the gradient method (Summa et al., 2013) and the Wavelet Covariance  
164 Transform (WCT) method (Baars et al., 2008) were employed. Further details on PBLH  
165 calculations can be found in Rathore et al., (2025). An automatic weather station (AWS) by  
166 Geonica, installed on the I-Tech building rooftop, collected meteorological data at 5-minute  
167 intervals. The data, including ambient temperature, relative humidity (RH), atmospheric  
168 pressure, wind speed and direction, precipitation, and incoming solar radiation, were retrieved  
169 using Datagraph-W4K 2.1.3.0 software and exported in CSV format. All sensors were  
170 meticulously calibrated and regularly cleaned to ensure accuracy and reliability.

171

## 172 **2.3 Auxiliary data**

### 173 **2.3.1 ObsPack Data**

174 To compare the seasonality of atmospheric CO<sub>2</sub> of Sonipat with other non-Indian sites in the  
175 same latitudinal band, we used selected sites from the  
176 obspack\_co2\_1\_GLOBALVIEWplus\_v10.1\_2024-11-13 (Schuldt et al., 2024). The data was  
177 averaged for five years from 2018 to 2022 for all stations except Boulder Atmospheric  
178 Observatory, Colorado, (2011-2016), to compare the seasonality over different locations across  
179 the globe.

180

### 181 **2.3.2 Satellite CO<sub>2</sub> retrievals**

182 Along with the ground-based in situ CO<sub>2</sub> measurements at the Sonipat monitoring station, we  
183 also used column average dry air CO<sub>2</sub> mole fraction (XCO<sub>2</sub>) retrievals from the Orbiting  
184 Carbon Observatory-2 and 3 satellites (OCO-2 and OCO-3) (Crisp et al., 2017; Eldering et al.,  
185 2017). We used the bias-corrected OCO-2 v11.1r data product for the period from February  
186 2023 to December 2024. The OCO-3 satellite provides XCO<sub>2</sub> data at a repeat cycle of 16 days  
187 with a spatial resolution of 1.60 km × 2.25 km (nadir observation), which increases the swath  
188 area from ~3.0 km<sup>2</sup> to ~3.5 km<sup>2</sup>. We used the bias-corrected OCO-3 v10.4r data product  
189 (Eldering et al., 2019; Srivastava et al., 2020) for the period from February 2023 to December  
190 2024.

191

### 192 **2.3.3 FluxSat GPP**

193 To study the Gross Primary Production (GPP) fluxes over Sonipat, we used FluxSat v2.2 native  
194 GPP product computed at the spatio-temporal resolution of the MCD43C data set (daily at  
195 0.05° spatial resolution (Schaaf et al., 2002; Wang et al., 2018). FluxSat v2.2 has been derived

196 from the MODerate resolution Imaging Spectroradiometer (MODIS) instruments on the NASA  
197 Terra and Aqua satellites using the collection 6.1 MCD43C Bidirectional Reflectance  
198 Distribution Function (BRDF)-Adjusted Reflectances (NBAR) (Joiner et al., 2018; Joiner and  
199 Yoshida, 2020; Schaaf and Wang, 2021). FluxSat v2.2 is “calibrated” using a set of the  
200 FLUXNET 2015 and OneFlux tier 1 (publicly released) eddy covariance (EC) data and has  
201 been compared with independent data (i.e., not used in the calibration) as validation. We used  
202 Global Gross Primary Production (GPP) estimates for 2023 in this study.

203

### 204 **2.3.4 Ecosystem-proxy variables**

205 We used two key ecosystem proxy variables to examine the carbon cycle dynamics at the  
206 Sonipat station and in the IGP region. The Normalised Difference Vegetation Index (NDVI)  
207 version 5 data from the Advanced Very High Resolution Radiometer (AVHRR) was used here  
208 (Vermote and NOAA CDR Program, 2018). The NDVI CDR summarises surface vegetation  
209 coverage activity based on measurements in the red and near-infrared spectral bands at daily  
210 intervals and at a spatial resolution of  $0.05^\circ \times 0.05^\circ$ .

211 To understand the photosynthetic capacity of the regional ecosystem to assimilate  
212 atmospheric CO<sub>2</sub>, we used Solar-Induced Chlorophyll Fluorescence (SIF) retrievals from the  
213 OCO-2 satellite (Frankenberg et al., 2014). The OCO-2 provides SIF data at a temporal  
214 resolution of 16 days and a spatial resolution of 1.35 km × 2.25 km. The estimation of SIF  
215 relies on evaluating the in-filling of solar Fraunhofer lines at 757 nm and 770.1 nm surrounding  
216 the O<sub>2</sub> A-band (Frankenberg et al., 2014; Sun et al., 2018). We used bias-corrected SIF data  
217 from OCO-2 v11r and v11.2r SIF data products.

218

## 219 **2.4 Models**

### 220 **2.4.1 JAMSTEC's MIROC version 4 atmospheric chemistry-transport model (MIROC4- 221 ACTM)**

222 We used the Model for Interdisciplinary Research on Climate version 4 (MIROC4),  
223 atmospheric general circulation model (AGCM)-based chemistry-transport model (MIROC4-  
224 ACTM; Patra et al., 2018), to simulate CO<sub>2</sub> mole fraction for this study. Simulations were  
225 performed at a horizontal resolution of T42 spectral truncations ( $\sim 2.8^\circ$  latitude–longitude grid)  
226 with 67 vertical hybrid-pressure layers between the Earth's surface and 0.0128 hPa ( $\sim 80$  km).  
227 CO<sub>2</sub> tracers were simulated corresponding to fossil fuel combustion (FFCO<sub>2</sub>), land biosphere  
228 fluxes (LBCO<sub>2</sub>), fire emissions (CO<sub>2fire</sub>), and ocean exchanges (CO<sub>2ocean</sub>) from different prior  
229 (bottom-up) emissions sets (Chandra et al., 2022). FFCO<sub>2</sub> was simulated using the gridded

230 fossil fuel emission dataset (GridFED; Jones et al., 2021). LBCO<sub>2</sub> tracers were simulated using  
231 two sets of terrestrial biosphere fluxes from the Carnegie-Ames-Stanford Approach (CASA)  
232 biogeochemical model (Randerson et al., 1997) and Vegetation Integrative Simulator for Trace  
233 Gases (VISIT) (Ito, 2019).

234

#### 235 **2.4.2 CarbonTracker (CT) inverse model**

236 To understand the temporal pattern of atmospheric CO<sub>2</sub> mole fraction over the study station  
237 and the IGP region, we used simulated CO<sub>2</sub> mole fraction from an inverse modelling  
238 framework CarbonTracker (CT) (Peters et al., 2005). Here, we used the CarbonTracker 2022  
239 release (CT2022), which incorporated two-way nesting of the offline atmospheric tracer  
240 transport model TM5, supporting coarse-resolution global data and high-resolution regional  
241 data (Krol et al., 2004). The TM5 model in CT2022 was driven with meteorology from the  
242 ERA-interim reanalysis provided by the European Center for Medium-Range Weather  
243 Forecasts (ECMWF). The CT2022 inverse model simulated atmospheric CO<sub>2</sub> mole fraction by  
244 correcting the prior specifications of CO<sub>2</sub> sources and sinks in the model by assimilating global  
245 in situ observations. In this study, we used the CT2022-simulated CO<sub>2</sub> mole fraction from  
246 February 2023 to October 2023.

247

#### 248 **2.4.3 GEOS-Chem inverse model**

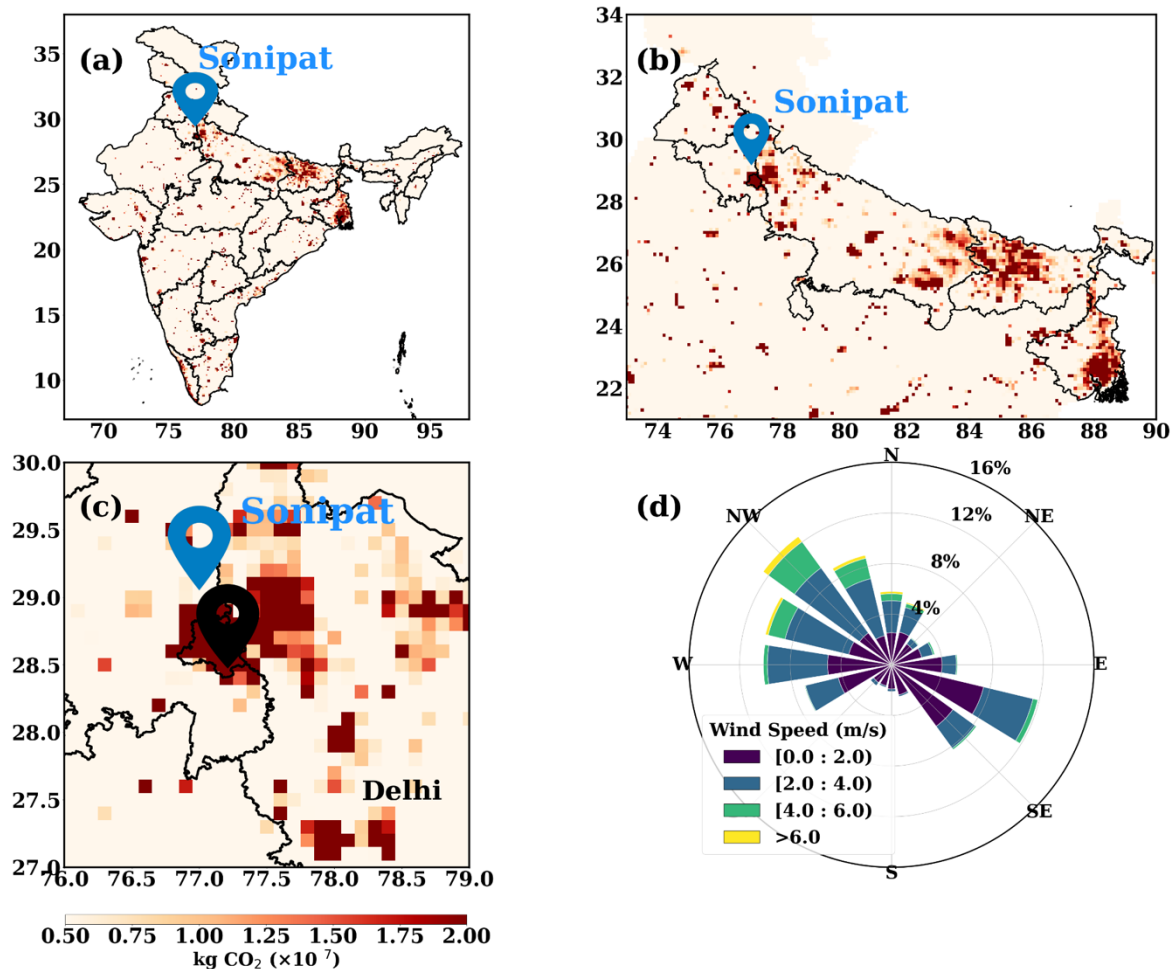
249 To study the seasonality of the fluxes over Sonipat, we used a four-dimensional variational  
250 (4D-Var) assimilation system with the GEOS-Chem global chemical transport model  
251 (CTM; Philip et al., 2019, 2022). The GEOS-Chem 4D-Var system was constrained with XCO<sub>2</sub>  
252 retrievals from the OCO-2 satellite (Philip et al., 2022), following the protocol of the OCO-2  
253 v10 Multi-model Intercomparison Project (MIP) (Byrne et al., 2017; Liu et al., 2014). The Net  
254 Ecosystem Exchange (NEE) fluxes for 2023 at a spatial resolution of 1° × 1°, constrained with  
255 the OCO-2 Land Nadir and Land Glint observational modes are used here.

256

#### 257 **2.4.4 Mi CASA terrestrial biospheric model**

258 We also used simulated CO<sub>2</sub> fluxes from a terrestrial biospheric model (TBM) in this study.  
259 The Más informada Carnegie-Ames-Stanford-Approach (Mi CASA) model (Weir, 2024), a  
260 comprehensive update to the CASA – Global Fire Emissions Database, version 3 (CASA-  
261 GFED3) product, was utilised here (Chen et al., 2023; Potter et al., 1993). Mi CASA provides  
262 daily global data at 0.1° resolution from January 2001 to December 2023. This includes carbon  
263 flux variables from sources such as net primary production (NPP), heterotrophic respiration

264 (Rh), wildfire emissions (FIRE), and fuel wood burning emissions (FUEL). The model is  
 265 driven with meteorological data from NASA's Modern-Era Retrospective analysis for Research  
 266 and Application, Version 2 (MERRA-2).



267  
 268 **Figure 1:** Anthropogenic CO<sub>2</sub> emissions over (a) India (b) IGP and (c) Sonipat/Delhi derived  
 269 from the EDGAR emission inventory for 2021. (d) Annually averaged wind patterns over  
 270 Sonipat for February 2023 – January 2024.

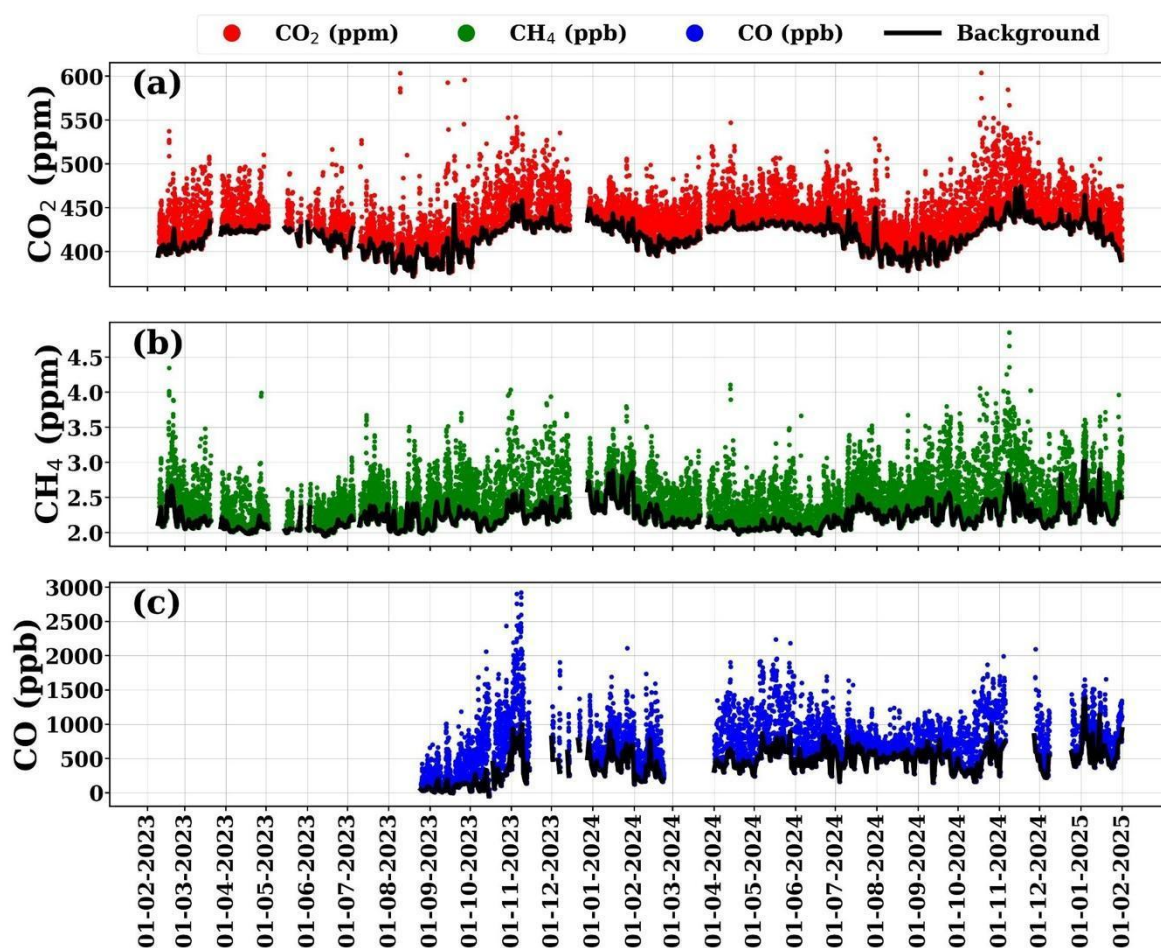
271  
 272

### 273 3. Results and discussions

#### 274 3.1 CO<sub>2</sub> measurements at Sonipat station

275 Figures 1(a-c) illustrate the annual mean anthropogenic CO<sub>2</sub> emissions over India, IGP and  
 276 Delhi/Sonipat for 2021 based on the EDGAR emission inventory, a major hotspot of  
 277 anthropogenic CO<sub>2</sub> emissions. The dominant wind direction over Sonipat was from the

278 northwest during the study period, highlighting influence from upwind sources of pollution and  
 279 greenhouse gases (Figure 1d). Seasonal changes in meteorological parameters (air temperature,  
 280 relative humidity, rainfall and wind; Figures S2 and S3) were also analysed alongside CO<sub>2</sub> to  
 281 better understand the role of meteorology in Sonipat. In this study, we focus on seasonal and  
 282 diurnal CO<sub>2</sub> variability and compare these patterns with those at other stations in India and in  
 283 the same latitudinal band across the globe to uncover the unique aspects of CO<sub>2</sub> dynamics over  
 284 Sonipat and the IGP.



285  
 286 **Figure 2:** (a) Hourly averaged time series of atmospheric (a) CO<sub>2</sub>, (b) CH<sub>4</sub>, and (c) CO mole  
 287 fraction for the study period (February 2023 to January 2025) over Sonipat. The thick black  
 288 line represents the background mole fraction estimated using the ADVS method. CO<sub>2</sub> and CH<sub>4</sub>  
 289 measurements were made using a Picarro GHG analyser, and CO measurements were made  
 290 using CUPI-G sensor

291  
 292 Figure 2 presents the hourly averaged time series of atmospheric (a) CO<sub>2</sub>, (b) CH<sub>4</sub>, and  
 293 (c) CO mole fractions at Sonipat during the study period (February 2023 to January 2025).

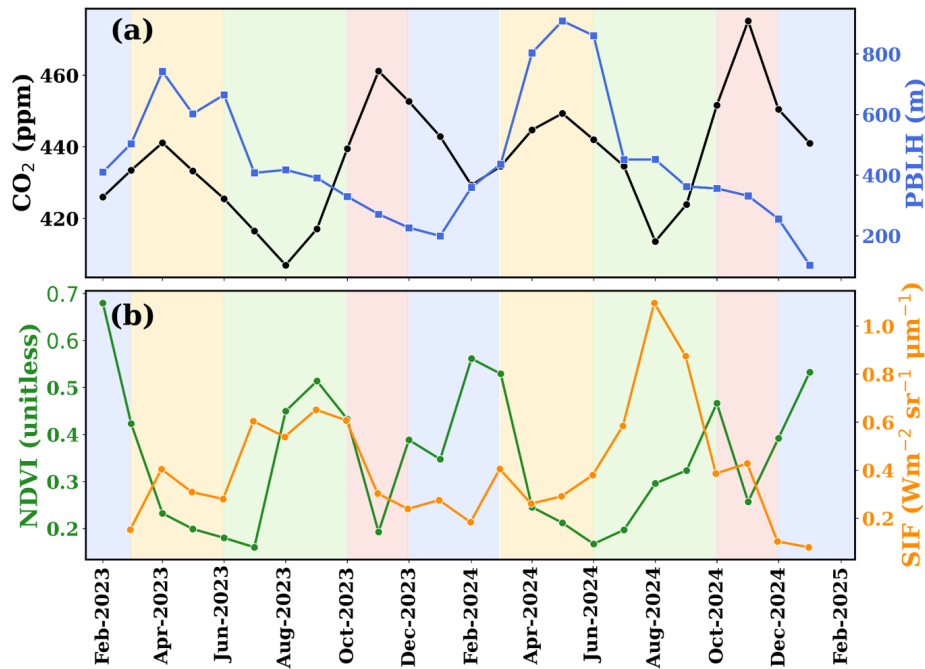
294 Hourly CO<sub>2</sub> mole fractions range from ~380 ppm to ~550 ppm, indicating strong monthly  
295 variations in CO<sub>2</sub> mole fractions at the monitoring station. The lowest CO<sub>2</sub> mole fractions were  
296 observed from July to August, which coincided with weak CO and strong CH<sub>4</sub> values. The  
297 highest mole fractions of CO<sub>2</sub> were observed from October to November, coinciding with the  
298 highest mole fractions of CO and CH<sub>4</sub>. We found an annual mean CO<sub>2</sub> mole fraction of  
299  $440.8 \pm 19.7$  ppm for 2024 and compared it with those from other monitoring stations across  
300 India (Table S1). Interestingly, despite differences in site characteristics, the annual mean CO<sub>2</sub>  
301 levels at rural stations like Gadanki and urban stations like Ahmedabad are comparable,  
302 whereas Sonipat shows distinctly higher values.

### 303 **3.2 Seasonal variability**

#### 304 **3.2.1 Seasonality of in situ observations**

305 Figure 3 shows the monthly mean atmospheric CO<sub>2</sub> mole fractions during the study period. A  
306 shaded background has been used to distinguish the seasonal regimes used in this study. The  
307 monthly mean CO<sub>2</sub> mole fraction shows a maximum in November (post-monsoon season) and  
308 a minimum in August (monsoon season) in both years. The observed seasonal mean of CO<sub>2</sub>  
309 during different seasons were  $440.8 \pm 19.7$  ppm (pre-monsoon),  $422.6 \pm 23.3$  ppm (monsoon),  
310  $456.4 \pm 30.8$  ppm (post-monsoon), and  $440.5 \pm 19.7$  ppm (winter).

311 The seasonal change in CO<sub>2</sub> mole fractions over the monitoring station is governed by  
312 the strength of emission sources, photosynthetic activity (biospheric fluxes), local meteorology  
313 and atmospheric transport. The planetary boundary layer height (PBLH), which is determined  
314 by local meteorology, strongly influences CO<sub>2</sub> mole fractions. PBL is the lowest layer within  
315 the troposphere, where temperature and wind speed variations are integral in modulating its  
316 height. During pre-monsoon, deep convection due to the well-developed PBLH from the  
317 surface to the upper troposphere results in lower mole fractions of CO<sub>2</sub>, while the weakly  
318 developed PBLH in winter leads to higher CO<sub>2</sub> (Baker et al., 2012; Kar et al., 2004; Park et al.,  
319 2009; Patra et al., 2011; Randel and Park, 2006).



320

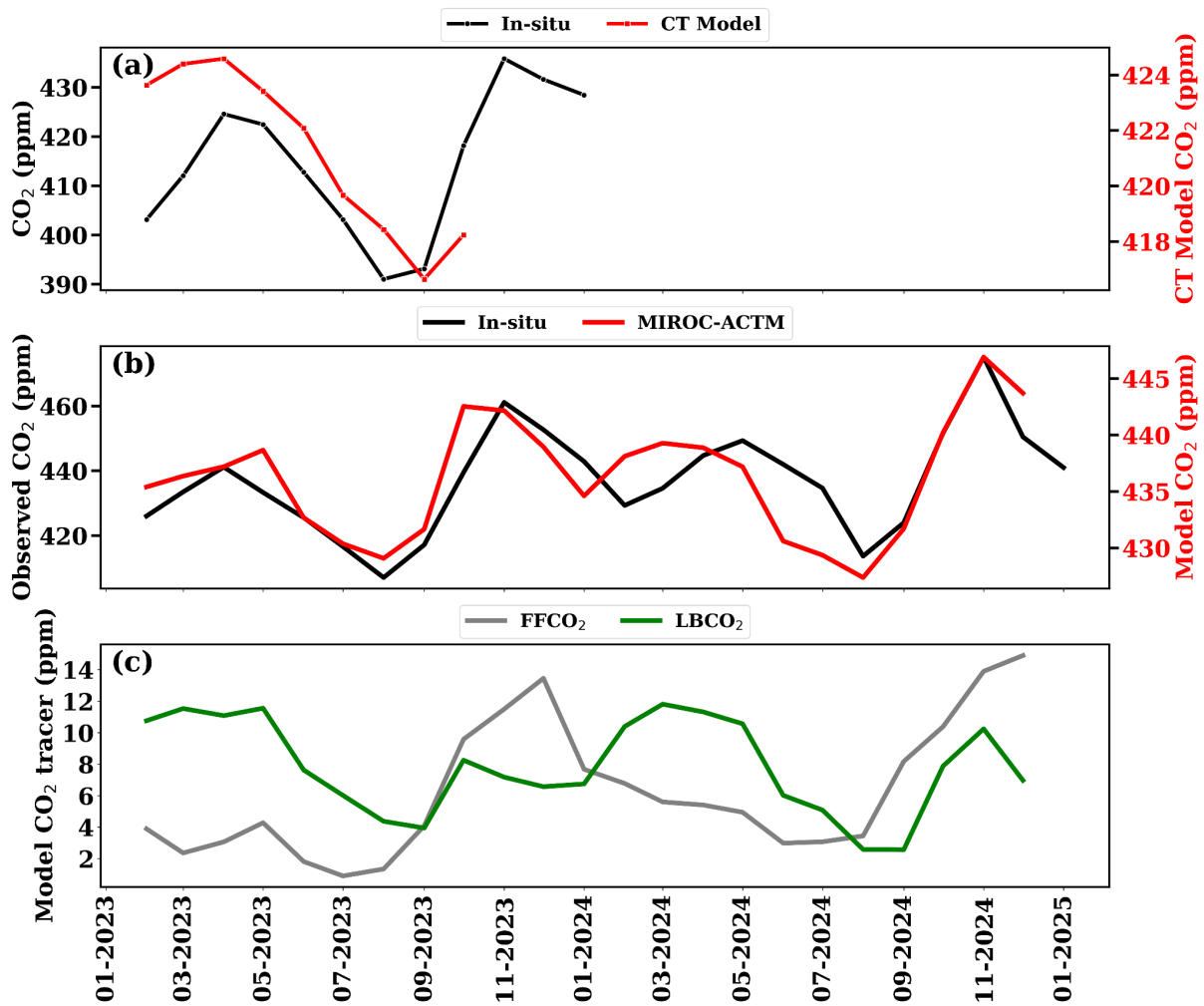
321 **Figure 3:** (a) Monthly variations of atmospheric CO<sub>2</sub> mole fraction (black) and PBLH (blue)  
 322 and (b) NDVI (green) and SIF (orange) over the Sonipat monitoring station during the study  
 323 period. The shaded background represents different seasons; yellow (pre-monsoon), green  
 324 (monsoon), red (post-monsoon) and blue (winter).

325 The seasonal change in CO<sub>2</sub> was examined using two different vegetation indices  
 326 (normalised difference vegetation index, NDVI and solar-induced fluorescence, SIF) to assess  
 327 the role of the biosphere in CO<sub>2</sub> mole fractions over Sonipat. Both NDVI and SIF have been  
 328 widely used as indicators of vegetation cover and photosynthetic activity (Aburas et al., 2015;  
 329 Nath, 2014). Our analysis shows a strong inverse relationship between CO<sub>2</sub> levels and NDVI,  
 330 as illustrated in Figure 3b. A noticeable decrease in atmospheric CO<sub>2</sub> mole fraction is observed  
 331 at the onset of the monsoon (June), with increased vegetative activity continuing until  
 332 September. Increased vegetation cover increases photosynthetic carbon uptake by the  
 333 biosphere. However, as vegetation activity decreases from the post-monsoon to winter and pre-  
 334 monsoon seasons, photosynthetic carbon uptake decreases, leading to a rise in atmospheric  
 335 CO<sub>2</sub>. Spearman's rank correlation analysis showed a weak and statistically insignificant  
 336 relationship between CO<sub>2</sub> and NDVI ( $\rho = -0.09$ ,  $p = 0.74$ ). In contrast, CO<sub>2</sub> exhibited a  
 337 moderate negative correlation with SIF ( $\rho = -0.42$ ,  $p = 0.07$ ). The negative correlation with  
 338 SIF is consistent with enhanced biospheric uptake during periods of increased photosynthetic  
 339 activity. Similar studies (Metya et al., 2021; Sreenivas et al., 2016; Tiwari et al., 2014), over  
 340 India exhibited a strong dependence of CO<sub>2</sub> seasonality on local vegetative carbon uptake.

341 A sharp decrease in the seasonal mean (~18 ppm) was noted from pre-monsoon to  
342 monsoon, attributed to enhanced photosynthetic activity around the measurement site, driven  
343 by abundant soil moisture. A further decrease in CO<sub>2</sub> mole fraction is also observed as the  
344 monsoon progresses, with minimum CO<sub>2</sub> mole fractions observed in August. The decreases in  
345 temperature (due to cloudy, overcast conditions prevailing during these months) reduce leaf  
346 and soil respiration, thereby enhancing carbon uptake (Jing et al., 2010; Patil et al., 2014).  
347 Further, an increase in CO<sub>2</sub> mole fraction (~34 ppm) is observed during post-monsoon,  
348 reflecting higher ecosystem respiration (Sharma et al., 2014) and enhanced soil microbial  
349 activity (Fan & Forkel, 2025; Munksgaard et al., 2022), particularly from nocturnal respiration  
350 prior to crop harvest. The gradual decline in NDVI during this period indicates reduced CO<sub>2</sub>  
351 uptake by vegetation. This season coincided with crop-burning episodes in northern India,  
352 which significantly increased CO<sub>2</sub> mole fractions. A sharp decrease (~16 ppm) in the seasonal  
353 mean during winter is evident compared to the post-monsoon. The shallow PBLH and winds  
354 from western IGP that transport crop-burning residue contribute to the enhanced mole fraction  
355 during winter. Table S2 compares the seasonal amplitude and the peak and drawdown months  
356 at the measurement site with those in similar studies across India. Sonipat exhibits higher  
357 seasonal amplitudes than other sites. However, a similar pattern in CO<sub>2</sub> peak and drawdown  
358 months is evident in other monitoring stations.

### 359 **3.2.2 Seasonal constraints from model and satellites**

360 Figure 4(a) shows the comparison of ground-based mole fraction of CO<sub>2</sub> with CarbonTracker  
361 inverse model (CT2022) simulated mole fraction (see different y-axis). The model outputs  
362 beyond October 2023 were not publicly available. In general, the CT2022 model-simulated  
363 mole fractions are much lower than the observed mole fractions at the Sonipat station. The  
364 discrepancy is mainly due to the model's coarser resolution. Nevertheless, the model-simulated  
365 seasonal pattern of CO<sub>2</sub> mole fraction is broadly in agreement with observations (Figure 4).  
366 The CT2022 model simulates a minimum mole fraction of 416 ppm in September, whereas in  
367 situ measurements show a minimum of 407 ppm in August. The CT2022 model exhibits higher  
368 mole fractions during the pre-monsoon season, consistent with in situ data. Note that most  
369 global and regional chemical transport models were unable to reproduce the large seasonal  
370 amplitude of surface-based measured atmospheric CO<sub>2</sub> mole fractions at any of the monitoring  
371 stations in India with different ecosystems (Lin et al., 2018; Philip et al., 2022).



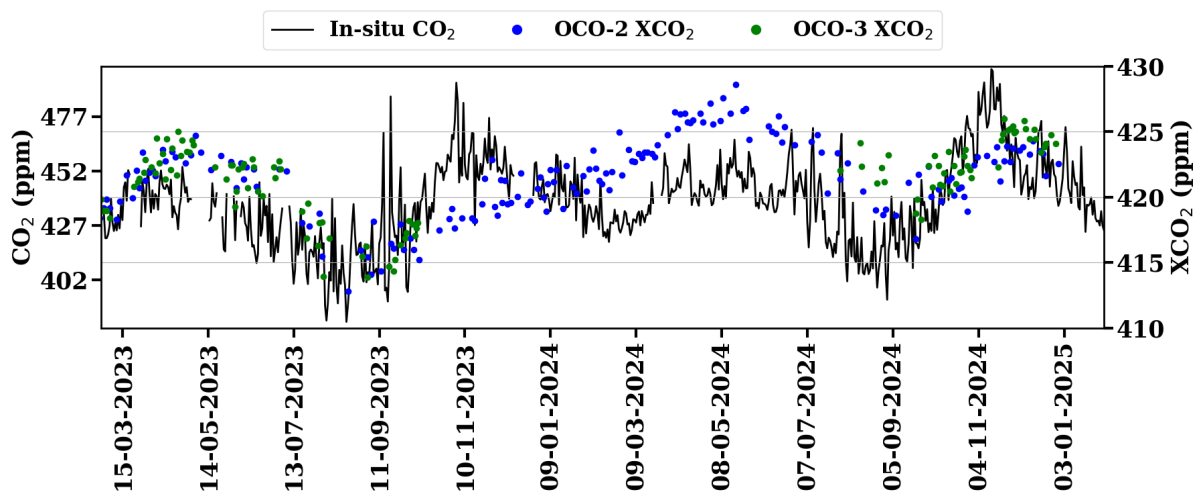
372

373 **Figure 4:** (a) Monthly mean background CO<sub>2</sub> mole fraction over Sonipat (estimated using the  
 374 ADVS method) compared to CarbonTracker (CT2022) model-simulated values at daytime  
 375 (13:00 – 16:00). Note that the left y-axis represents surface mole fraction from in situ  
 376 measurements, and the right y-axis represents CT2022-simulated mole fraction. (b) comparison  
 377 of simulated mole fraction of atmospheric CO<sub>2</sub> from MIROC-ACTM with in situ  
 378 measurements at Sonipat and (c) monthly averaged time series of different tracers from the  
 379 MIROC-ACTM.

380

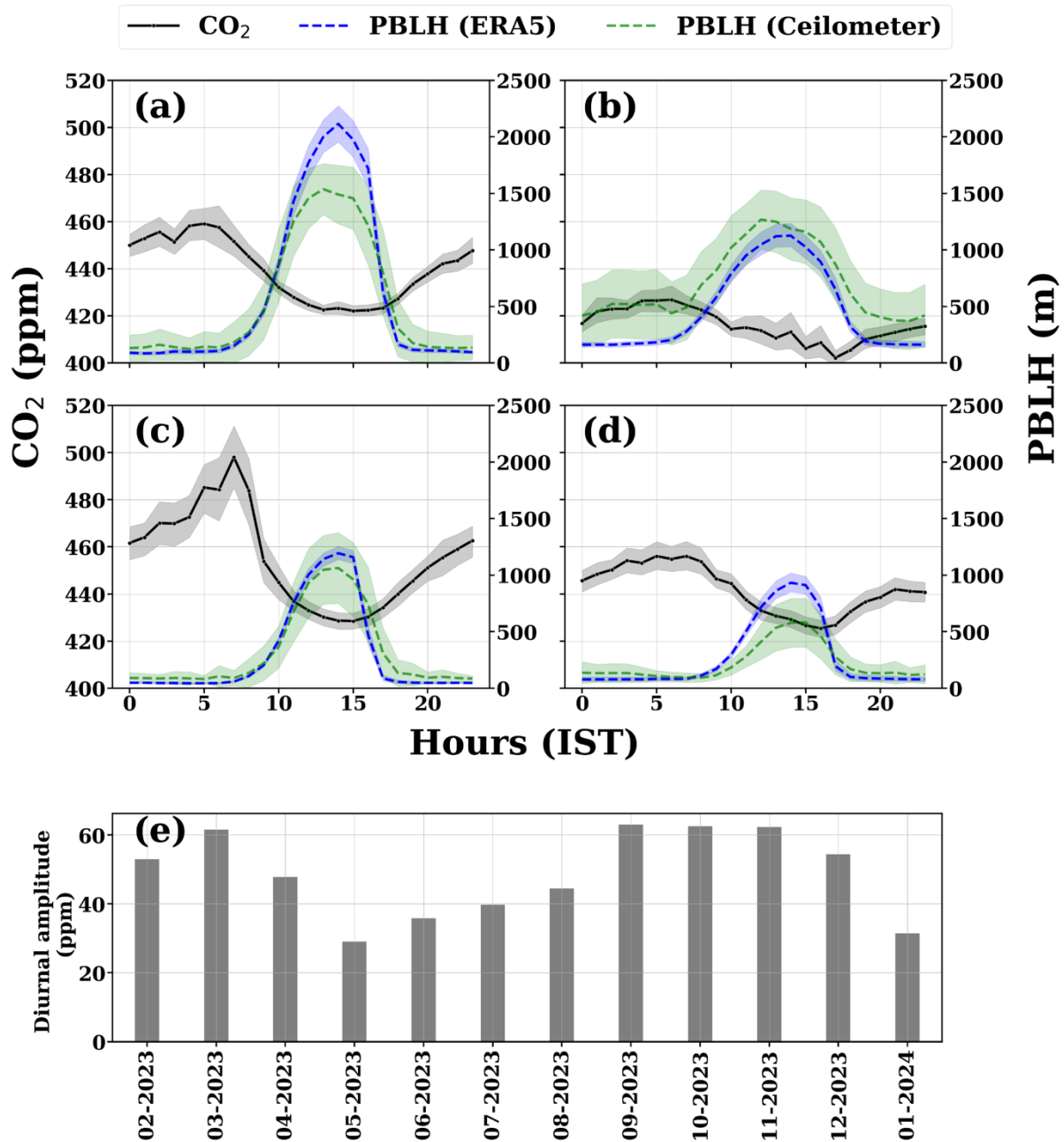
381 Figure 4(b) shows the comparison of atmospheric CO<sub>2</sub> mole fractions over Sonipat with  
 382 the simulated mole fraction of CO<sub>2</sub> from the MIROC4-ACTM model. Similar to CT2022,  
 383 MIROC captures the seasonal pattern of CO<sub>2</sub>, but fails to capture the actual seasonal amplitude  
 384 over Sonipat. Figure 4(c) presents the monthly averaged time series of model-simulated CO<sub>2</sub>  
 385 tracers. The fossil fuel tracer (FFCO<sub>2</sub>) exhibits a peak in the post-monsoon period, followed by  
 386 a gradual decrease through the end of winter. The shallow PBLH during this time traps  
 387 vehicular emissions from NH-44 and industrial sources upwind of the monitoring station,

388 resulting in higher FFCO<sub>2</sub>. With the development of the PBLH in the pre-monsoon, FFCO<sub>2</sub>  
 389 shows a gradual decrease, and rainfall during the monsoon results in minimum values during  
 390 this time. The biospheric tracer (LBCO<sub>2</sub>) shows a peak during the pre-monsoon, driven by dry  
 391 soil conditions and a lack of vegetation and a drawdown during the monsoon. A sharp increase  
 392 in LBCO<sub>2</sub> is observed during the post-monsoon season, coinciding with the harvest period at  
 393 the monitoring station. Being surrounded by agricultural land, Sonipat is prone to emissions  
 394 from crop residue burning around and upwind of the monitoring station. Both models  
 395 underestimate these enhancements from regional sources.



396  
 397 **Figure 5:** Daily variations of atmospheric CO<sub>2</sub> mole fraction from in situ measurements over  
 398 Sonipat (left y-axis) with column average CO<sub>2</sub> mole fraction (XCO<sub>2</sub>) from the OCO-2 (ppm)  
 399 and OCO-3 (ppm) satellite instruments (right y-axis).

400  
 401 Figure 5 compares XCO<sub>2</sub> from OCO-2 and OCO-3 satellites with ground-based CO<sub>2</sub>  
 402 measurements at Sonipat during the study period. XCO<sub>2</sub> reveals a similar seasonal pattern with  
 403 high mole fraction during the pre-monsoon season, followed by a drawdown in CO<sub>2</sub> mole  
 404 fraction during the monsoon season and a further gradual increase in CO<sub>2</sub> during the post-  
 405 monsoon and winter. Although the satellite column data captures the monthly variability  
 406 reasonably well, it fails to capture the sharp increase in mole fraction during the post-monsoon.  
 407 This post-monsoon enhancement from crop residue burning at the monitoring station, along  
 408 with additional transport from Punjab, highlights the limitations of high-resolution satellite data  
 409 in capturing local enhancements.



410  
 411 **Figure 6:** (a-d) Seasonally-averaged diurnal variation of atmospheric CO<sub>2</sub> over the Sonipat  
 412 station during the pre-monsoon (MAM), monsoon (JJAS), post-monsoon (ON) and winter  
 413 (DJF) seasons with planetary boundary layer heights (blue denotes PBLH from ERA5 and  
 414 green denotes PBLH derived from Ceilometer), (e) monthly variation of the diurnal amplitude  
 415 of CO<sub>2</sub> from February 2023 to January 2024.

416

### 417 3.3 Diurnal variability

418 Figure 6 (a-d) presents the averaged diurnal variation of atmospheric CO<sub>2</sub> mole  
 419 fractions along with PBLH from ERA5 and Ceilometer at Sonipat during four seasons for the

420 first year of the study (February 2023 – January 2024). Figure S5 presents the diurnal variation  
421 for the second year of the study. The diurnal cycle has been analysed separately for each year,  
422 combining available PBLH data. All seasons exhibit a similar diurnal pattern, with maximum  
423 CO<sub>2</sub> mole fractions in the early morning hours (05:00 - 08:00 am) and minimum mole fractions  
424 in the late afternoon hours (2:00 - 3:00 pm). The observed diurnal cycle of CO<sub>2</sub> is closely  
425 associated with the development of PBLH during the day (Figure 6). The peak in CO<sub>2</sub> mole  
426 fraction during the morning hours can be attributed to the fumigation effect, and a well-mixed  
427 PBL dilutes CO<sub>2</sub> mole fractions during the afternoon hours.

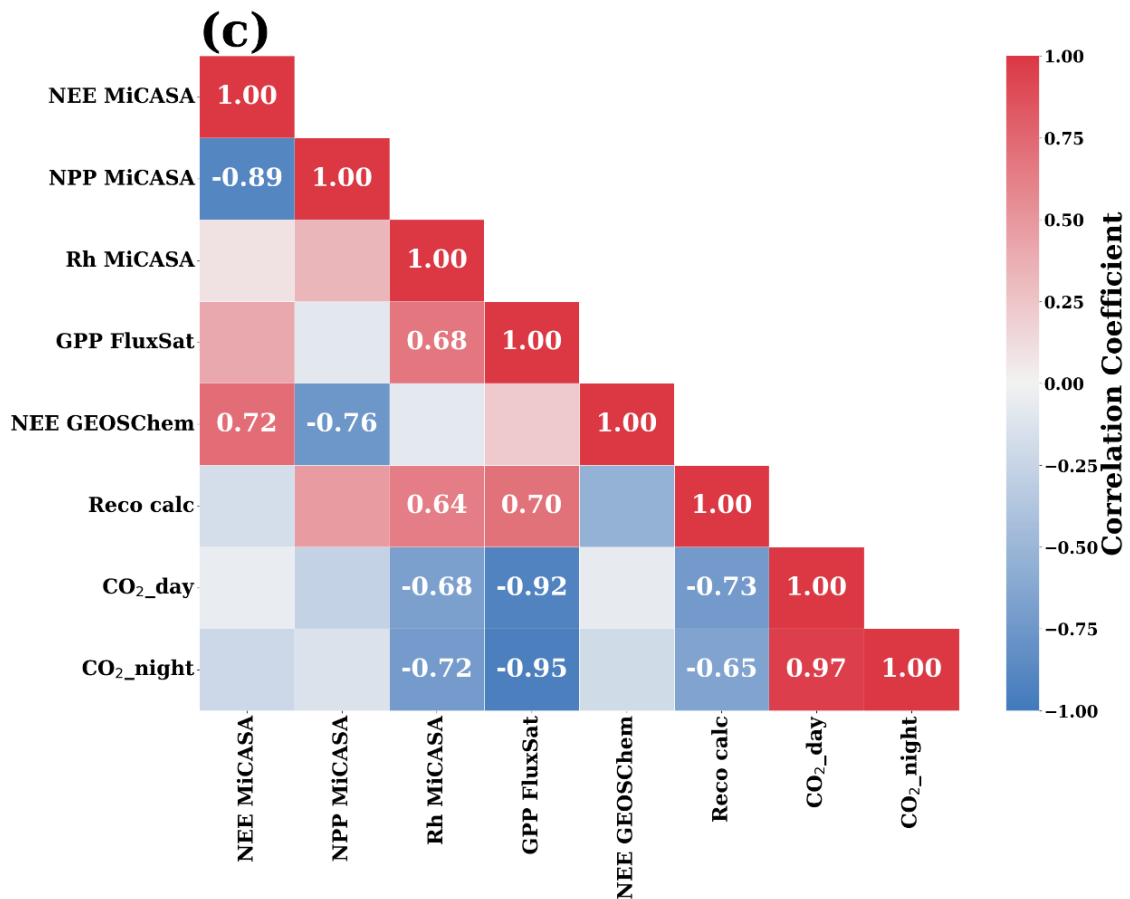
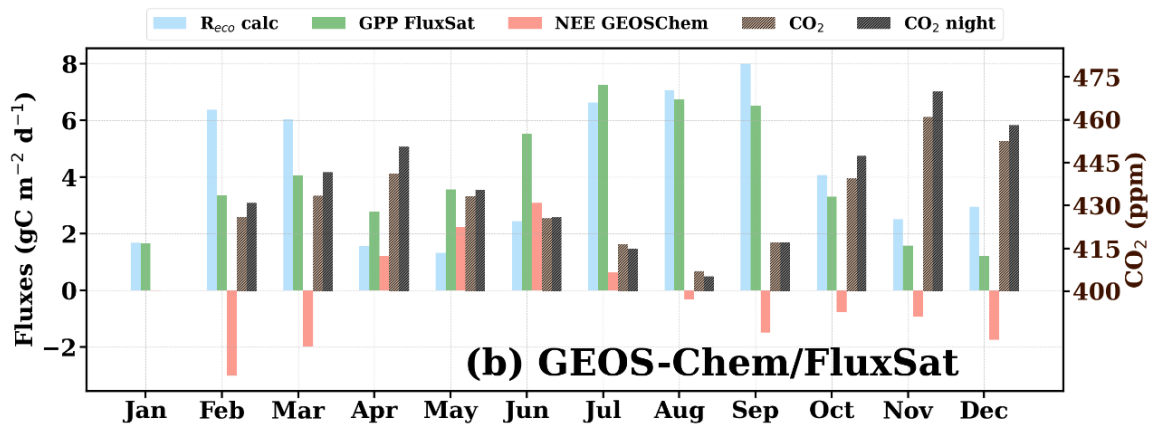
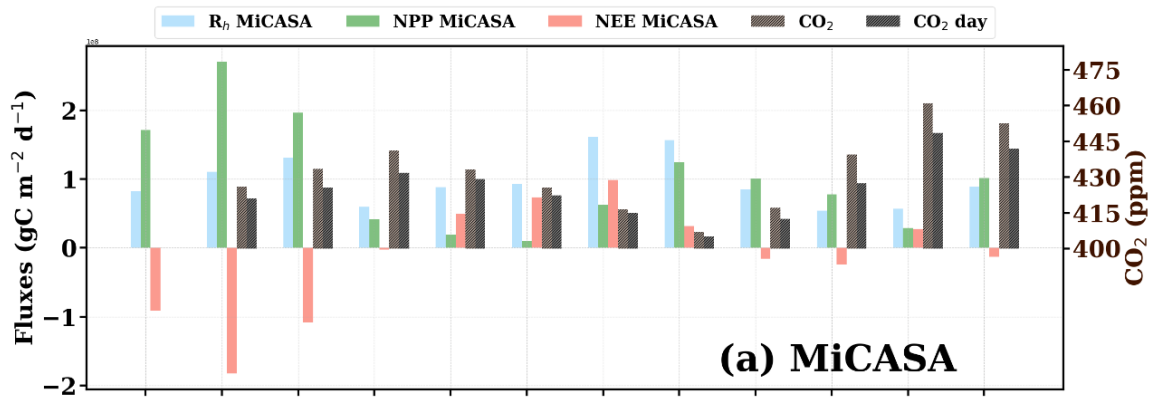
428         Photosynthetic activity is another key driver of diurnal variability at Sonipat, a  
429 characteristic observed in rural areas with vegetative cover (Imasu & Tanabe, 2018). Strong  
430 vegetative uptake of CO<sub>2</sub> during the monsoon results in minimum daytime CO<sub>2</sub> mole fractions,  
431 and the lack of vegetation during post-monsoon contributes to maximum daytime CO<sub>2</sub> mole  
432 fractions during this season. The diurnal variation of GHGs reported by several studies  
433 (Nishanth et al., 2014; Patil et al., 2014; Sharma et al., 2014) from different parts of the country  
434 shows a similar trend. The same was observed for 2024 as well (Figure S5). The diurnal  
435 variability of CO<sub>2</sub> over Sonipat is driven by biospheric activity and local meteorology.

436 Figure 6(e) shows the monthly average variation in diurnal amplitude (difference between the  
437 maximum and minimum mole fraction of CO<sub>2</sub> in the diurnal cycle) during the first year. The  
438 lowest diurnal amplitude of about 29 ppm is observed in May, while the highest amplitude at  
439 about 63 ppm is observed in September/October. We found that the post-monsoon season  
440 exhibited the highest diurnal variability (~60 ppm), followed by the pre-monsoon (~35 ppm),  
441 winter (~30 ppm), and monsoon (~20 ppm) seasons.

442

### 443 **3.4 Drivers of CO<sub>2</sub> seasonality**

444         The contribution of biospheric fluxes in driving the CO<sub>2</sub> mole fraction over Sonipat (for  
445 2023) was analysed in Figure 7. Figure 7(a) shows the simulated data from the Mi CASA  
446 biosphere model along with the monthly averaged mole fractions of CO<sub>2</sub> and daytime CO<sub>2</sub>  
447 (06:00 – 18:00). Figure 7(b) presents the simulated NEE from GEOS-Chem and GPP from  
448 FluxSat, along with the monthly averaged mole fractions of daily-mean and nighttime CO<sub>2</sub>  
449 (18:00 – 06:00). Positive NEE values indicate a net exchange of CO<sub>2</sub> from the biosphere to the  
450 atmosphere. On the other hand, a negative NEE value (when NPP exceeds Rh) suggests the  
451 uptake of CO<sub>2</sub> from the atmosphere to the biosphere.



453 **Figure 7:** Monthly variation of atmospheric CO<sub>2</sub> mole fraction (for 2023) over the Sonipat  
454 monitoring station compared against (a) biospheric fluxes from the MiCASA terrestrial  
455 biospheric model and (b) GEOS-Chem model and FluxSat GPP data. (a - b) The CO<sub>2</sub> mole  
456 fraction are daytime-mean (06:00 - 18:00 LT) and night time-mean (18:00 - 06:00 LT). The  
457 correlation heatmap of all the variables. The annual growth rate of CO<sub>2</sub> has been subtracted  
458 from the CO<sub>2</sub> mole fraction using background data from the Mauna Lou observatory. The  
459 variable “Reco calc” was calculated as the difference between NEE (GEOS-Chem) and GPP  
460 (FluxSat). The Pearson correlation coefficients with a p value less than 0.05 have been  
461 displayed in the correlation plot.

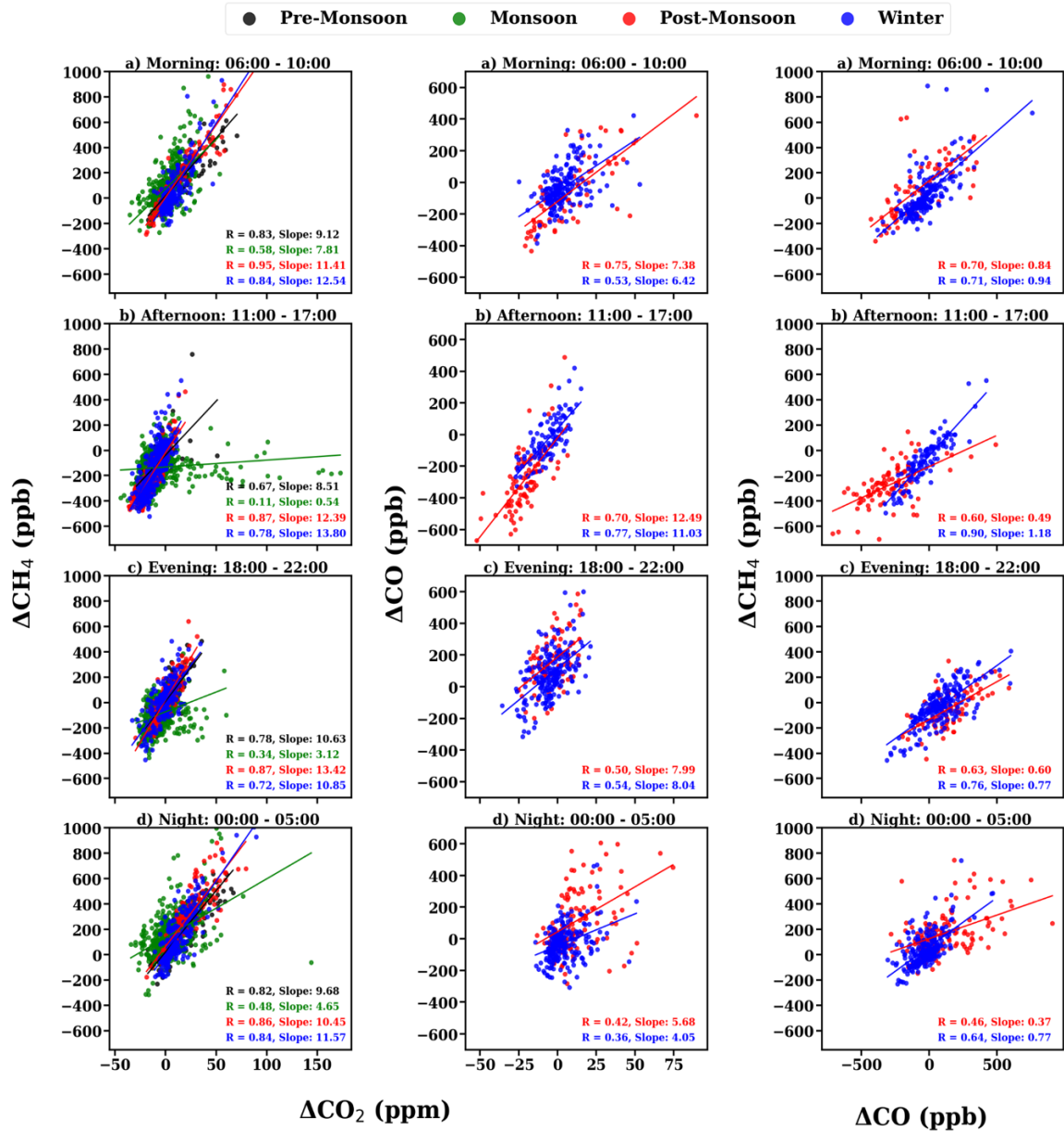
462

463 The NEE flux shows a strong positive in June, followed by a gradual decrease through  
464 October (monsoon). During this time, Reco, Rh and GPP exhibit strong enhancements. These  
465 enhancements are accompanied by a drawdown of CO<sub>2</sub> during this time. The driving factor  
466 behind this CO<sub>2</sub> drawdown during monsoon is the enhanced ecosystem productivity during this  
467 time. Strong inverse correlations of GPP, Rh, and Reco with CO<sub>2</sub> suggested that the biosphere  
468 acts as a net sink of CO<sub>2</sub> (Figure 8c).

469 Interestingly, post-monsoon and winter months exhibit weak or negative NEE. This is  
470 because Rh values are low during these seasons due to drier soil conditions and lower soil  
471 moisture. It is also notable that GPP is very low during these months, which is associated with  
472 a high CO<sub>2</sub> mole fraction. Significant contributions of air-mass transport from upwind regions  
473 and boundary-layer dynamics, along with the lack of vegetation during this time, contribute to  
474 the buildup of CO<sub>2</sub> mole fraction.

475

476



477

478 **Figure 8:** Tracer-tracer relations of  $\Delta\text{CO}_2 / \Delta\text{CH}_4$  (left panel),  $\Delta\text{CO}_2 / \Delta\text{CO}$  (middle panel) and  
 479  $\Delta\text{CH}_4 / \Delta\text{CO}$  (right panel) during a) Morning (0600–1000 IST), b) afternoon (1100–1700 IST),  
 480 c) evening (1800–2200 IST) and d) night (0000–0500 IST).

481

### 482 3.5 Emission source detection using tracer-tracer relationships

483 The ratios (tracer-tracer) of GHGs have been widely used in previous studies to estimate  
 484 different emission source contributions to atmospheric GHGs (Chandra et al., 2016, 2019; Lin  
 485 et al., 2015; Lopez, 2012; Paris et al., 2008; Sreenivas et al., 2016, 2022). We followed a similar  
 486 tracer-tracer correlation analysis to assess synoptic variation in CO<sub>2</sub> across different diurnal  
 487 time windows and understand the emission sources contributing to CO<sub>2</sub> mole fractions over

488 Sonipat (Figure 8). The measurements have been divided into four-time windows: (a) morning  
489 hours (06:00 - 10:00; the PBLH starts to develop after sunrise; local traffic is high), (b)  
490 afternoon hours (11:00 - 17:00; the PBLH is well-developed; relatively minimum local traffic,  
491 (c) evening hours (18:00 - 22:00; rush hour traffic and high household emissions), and (d) night  
492 hours (00:00 - 00:05; relatively less anthropogenic emission sources). Excess mole fractions  
493 were used in the correlation analysis to remove the influence of background mole fractions on  
494 the correlation ratios (Worthy et al., 2009). The correlation between the different gases (CO<sub>2</sub>,  
495 CH<sub>4</sub>, and CO) has been studied using the robust linear fit regression method.

496

497 Figure 8 (left panel) presents the correlation of excess mole fraction of CH<sub>4</sub> and CO<sub>2</sub>  
498 during the four seasons. The CH<sub>4</sub>/CO<sub>2</sub> correlation reveals a strong correlation ( $r > 0.6$ ) for all  
499 seasons except monsoon during all time windows, which suggests a similar source mechanism  
500 or a controlling emission process for both gases at the measurement site. Around the monitoring  
501 station, vehicular emissions from the nearby highway and natural gas combustion emissions  
502 are possible sources. Also, a positive correlation suggests that anthropogenic emissions  
503 dominate the carbon cycle in Sonipat (Fang et al., 2015). The regression slope shows strong  
504 diurnal variation throughout all seasons. Recent studies across India have reported similar  
505 results, with higher regression slopes during the post-monsoon and winter seasons than during  
506 the pre-monsoon and monsoon seasons (Lin et al., 2015; Sreenivas et al., 2016, 2022).

507

508 Figure 8 (middle panel) presents the correlation of excess mole fractions of CO and  
509 CO<sub>2</sub> during post-monsoon and winter. The CO/CO<sub>2</sub> ratio over Sonipat (4 – 12.5 ppb ppm<sup>-1</sup>) is  
510 lower than that for fresh plumes from wildfire (Andreae and Merlet, 2001; Mauzerall et al.,  
511 1998) and much lower than that from biomass burning events alone (Matsueda et al., 1999).  
512 Lin et al. (2015) reported CO/CO<sub>2</sub> ratios of 13 ppb ppm<sup>-1</sup> over Southeast Asian outflow from  
513 February to April 2001. This value was found to be influenced by fossil fuel emissions (Russo  
514 et al., 2003), crop residue burning, and biofuel burning rather than solely by biomass/biofuel  
515 burning. The CO/CO<sub>2</sub> ratios over Sonipat during the post-monsoon and winter closely match  
516 those of Lin et al. (2015), suggesting that the high CO<sub>2</sub> mole fractions during this time are an  
517 interplay of different sources like crop residue burning (long-range transport) and other fossil-  
518 fuel emissions (vehicular and industrial) around the monitoring station.

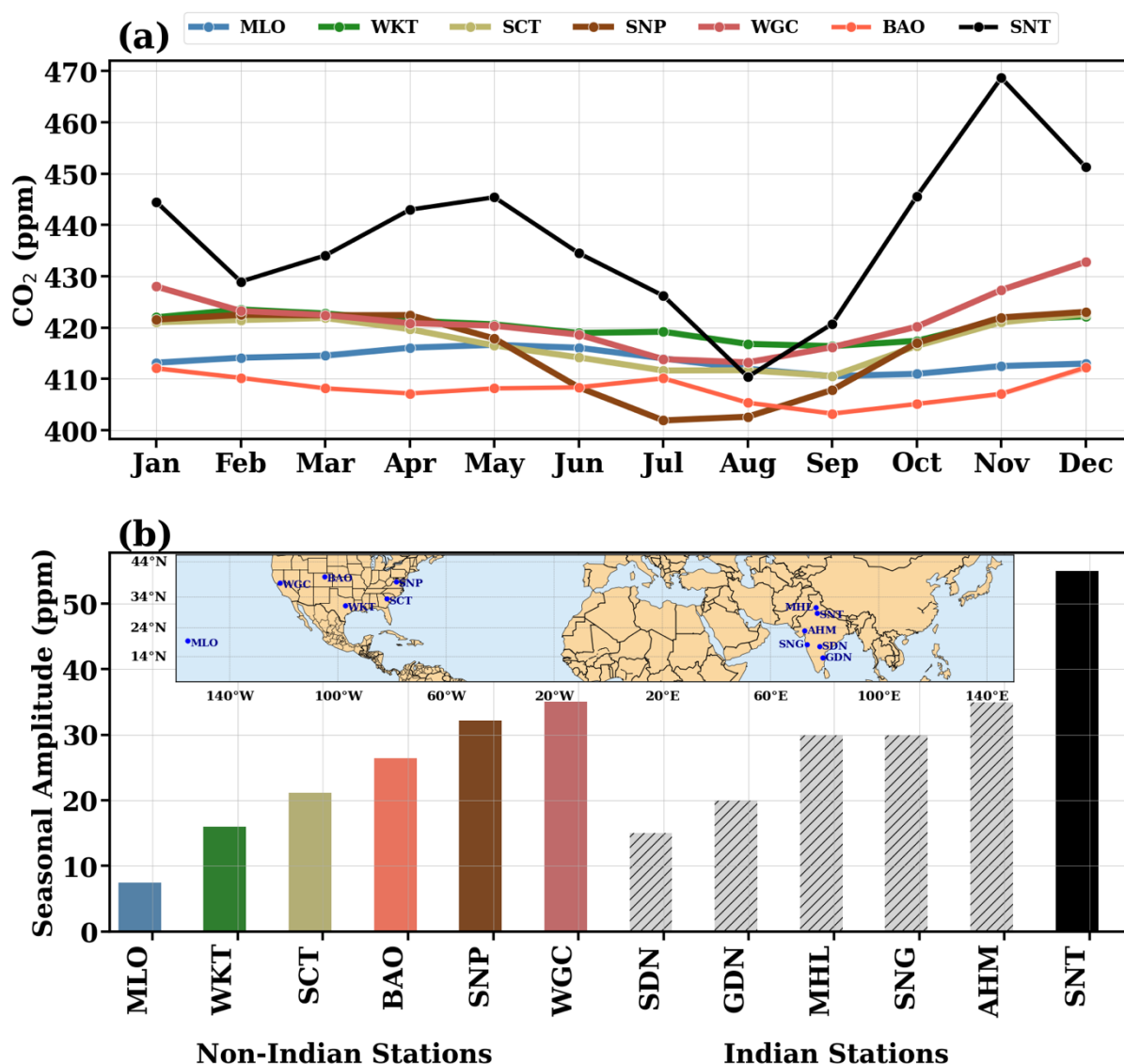
519

520 Figure 8 (right panel) presents the correlation of excess mole fractions of CH<sub>4</sub> and CO during  
521 post-monsoon and winter. The CH<sub>4</sub>/CO ratios range from 0.3 to 1.2 at Sonipat, indicative of

522 anthropogenic emission sources (Bakwin et al., 1995; Harriss et al., 1994; Lai et al., 2010; Lin  
 523 et al., 2015; Niwa et al., 2012; Sawa et al., 2004; Wada et al., 2011; Xiao et al., 2004). In  
 524 contrast, ratios influenced solely by biomass and biofuel burning are much lower, ranging from  
 525 0.07 to 0.3 (Andreae and Merlet, 2001; Mauzerall et al., 1998; Mühle et al., 2002).

526 These lower ratios highlight the significant difference when compared to the values  
 527 recorded in Sonipat. Moreover, very high CH<sub>4</sub> emissions from livestock can elevate the  
 528 generally low CH<sub>4</sub>/CO ratios associated with biomass burning. This indicates substantial  
 529 contributions from various CH<sub>4</sub> sources apart from biofuel burning.

530



531 **Figure 9:** (a) Comparison of the seasonal variability of atmospheric CO<sub>2</sub> over Sonipat  
 532 monitoring station with various locations in the same latitudinal band. (b) Comparison of the  
 533 seasonal amplitude between Indian (coloured bars) and international monitoring stations (grey  
 534 bars). Indian stations include Shadnagar (SDN), Sinhadgad (SNG), Ahmedabad (AHM), Mohali  
 535 bars).

536 (MHL), Gadanki (GDN), and Sonipat (SNT). International stations include Mauna Loa (MLO),  
537 South Carolina (SCT), Shenandoah National Park (SNP), Walnut Grove, (WGC), Moody  
538 (WKT) and Boulder (BAO). For all international stations except BAO, the five-year average  
539 (2018 - 2022) has been chosen for the seasonality. For BAO, 2011 – 2016 has been used due  
540 to lack of coinciding data. The monthly average of the entire study period (February 2023 –  
541 January 2025) has been used for this comparison.

542

#### 543 **4. Discussions**

544 By investigating two years of high-frequency atmospheric CO<sub>2</sub> mole fraction measurements at  
545 the Sonipat station in the IGP region, we identified the following salient features about the  
546 seasonality, diurnal variability, drivers of temporal variability, and emission sources of CO<sub>2</sub>.

547 **Very high atmospheric CO<sub>2</sub> mole fractions over IGP:** The surface-based  
548 measurements of atmospheric CO<sub>2</sub> mole fraction exhibit strong seasonality, with a maximum  
549 (456.4 ppm) during post-monsoon and a minimum (407.2 ppm) during monsoon, with an  
550 average of 422.6 ppm. Seasonal changes in the PBLH affected the atmospheric CO<sub>2</sub> mole  
551 fraction by diluting or concentrating GHG mole fractions near the surface. A strong dependence  
552 of CO<sub>2</sub> seasonality on local vegetative carbon uptake was observed from the negative  
553 correlation between NDVI and CO<sub>2</sub> mole fractions, which was consistent across India (Metya  
554 et al., 2021; Sreenivas et al., 2016; Tiwari et al., 2014).

555 A comparison of the seasonality of atmospheric CO<sub>2</sub> at Sonipat with other Indian and  
556 global sites in the same latitudinal band revealed very high seasonality at Sonipat, surpassing  
557 that of all other stations. This high seasonality is attributed to elevated CO<sub>2</sub> mole fractions in  
558 November (post-monsoon), driven by local emissions and crop residue burning. Figure 9a  
559 presents the monthly averaged variation of CO<sub>2</sub> over Sonipat during the study period (SNT)  
560 with other measurement sites in the same latitudinal band (5° N – 40° N). Details of all  
561 monitoring stations used in this study are described in detail in S1. Sonipat exhibits a very high  
562 seasonal amplitude (~60 ppm) compared to other sites worldwide (~15 ppm, see Figure 9b),  
563 attributed to the sharp increase in post-monsoon, consistent in both years of the study (see  
564 Figure 2). Excluding November would reduce the seasonal amplitude of Sonipat to 35 ppm,  
565 which is comparable to that in Ahmedabad (35 ppm). Temperature-driven PBLH (which  
566 inhibits mixing) and strong north-westerly winds (which induce transport of emissions from  
567 upwind) during this season play a key role in these high CO<sub>2</sub> mole fractions (Figure S3 and

568 S4). It is also noted that the CO<sub>2</sub> drawdown in August is primarily due to the green paddy fields  
569 during the monsoon (terrestrial CO<sub>2</sub> uptake), coinciding with heavy rains that wash out CO<sub>2</sub>.  
570 This combined effect makes the lowest CO<sub>2</sub> mole fractions in Sonipat comparable to those at  
571 some background stations across the globe with different ecosystems (Figure 9a).

572 This study also analysed the drivers of this variability using various ecosystem variables,  
573 including NEE, which represents the net carbon exchange between terrestrial ecosystems (the  
574 difference between Rh and NPP). NPP is the net amount of CO<sub>2</sub> retained in the biosphere. Rh  
575 is the amount of CO<sub>2</sub> emitted into the atmosphere due to the decomposition of organic matter  
576 by microorganisms in the soil. Reco, the sum of Ra (autotrophic respiration) and Rh has been  
577 calculated as the difference of FluxSat GPP and GEOS-Chem NEE. GPP, a measure of carbon  
578 uptake by plants, was observed to be very high during monsoon along with NEE, Rh and Reco.  
579 Statistical analysis revealed a strong negative correlation of GPP with CO<sub>2</sub> and a strong positive  
580 correlation with Rh and Reco. These suggest that the primary sink of CO<sub>2</sub> over Sonipat is  
581 biospheric activity, driven by the abundance of vegetation resulting from enhanced soil  
582 moisture during the monsoon.

583 **Performance of models and satellites over IGP:** Although both the CarbonTracker  
584 and MIROC-ACTM models captured the broad seasonal pattern of CO<sub>2</sub> mole fractions, they  
585 substantially underestimated it. However, MIROC showed greater seasonal variability than  
586 CT2022, with post-monsoon highs and pre-monsoon drawdowns showing strong correlations  
587 with in situ measurements. Further analysis of the tracers from MIROC provides insights into  
588 the driving factors of this variability. The post-monsoon peak is attributed to vehicular  
589 emissions from the nearby highway and industrial sources upwind of the monitoring station.  
590 The drawdown in monsoon is attributed to the added soil moisture and increased CO<sub>2</sub> uptake  
591 by plants during this time. The location of the measurement site in IGP, downwind of Punjab,  
592 provides insights into this transport-induced enhancement. The OCO-2 and OCO-3 satellite  
593 XCO<sub>2</sub> retrievals also showed similar seasonal variability; however, the satellites could not  
594 capture CO<sub>2</sub> enhancements from local sources.

595 **Diurnal variability driven by meteorology:** The atmospheric CO<sub>2</sub> mole fraction at  
596 Sonipat exhibits a consistent diurnal pattern across seasons. It was observed that CO<sub>2</sub> mole  
597 fractions steadily increased throughout the night, reaching a peak in the early morning hours.  
598 This accumulation of CO<sub>2</sub> during the night-time can be attributed to the fumigation effect: a  
599 significant rise in surface mole fractions, notable during the early morning hours due to the

600 breakdown of the nocturnal inversion layer following sunrise (Stull, 1988). Weak winds and  
601 shallow PBLH enhance the fumigation effect. The combined effect of photosynthetic activity  
602 and mixing of PBLH during the afternoon hours drives the CO<sub>2</sub> mole fractions during different  
603 seasons. The diurnal amplitude shows large month-to-month variation with an increasing trend  
604 from May to September 2023 and a decreasing trend till February 2024. Figure S6 presents the  
605 seasonal variation of CO<sub>2</sub> compared with PBLH derived from Ceilometer and ERA5 reanalysis  
606 data for 2023. A slight shift in the timing of the morning peaks was observed from season to  
607 season, due to changes in sunrise time, which affected photosynthetic activity.

608 **Detecting emission source contributions:** Tracer-tracer relationships across different  
609 time periods during the post-monsoon and winter seasons were examined. Analysis reveals  
610 that CO<sub>2</sub> and CH<sub>4</sub> exhibit a strong positive correlation across all seasons, suggesting common  
611 sources for both gases. During monsoon season, the afternoon time window shows a weak  
612 correlation with other time windows, revealing distinct source and sink mechanisms for CO<sub>2</sub>  
613 and CH<sub>4</sub>, such as CH<sub>4</sub> loss via hydroxyl radical and CO<sub>2</sub> uptake by plants. The regression  
614 slope is higher during the post-monsoon and winter months, when reduced photosynthetic  
615 activity and the dominance of local emissions and long-range transport are observed. The  
616 lower values during pre-monsoon and monsoon are associated with the dominance of  
617 vegetation and terrestrial uptake of CO<sub>2</sub> by photosynthetic activity.

618 The CO/CO<sub>2</sub> correlation shows strong diurnal variability, suggesting the dominance of  
619 different source mechanisms throughout the day, with strong correlation during the morning  
620 and afternoon hours (suggesting a similar source) and weaker correlation during the evening  
621 and night hours (suggesting different sources). The post-monsoon season shows higher  
622 regression slopes due to reduced photosynthetic activity. Over Sonipat, the contribution of CO  
623 and CO<sub>2</sub> from long-range air mass transport (influenced by crop residue burning in Punjab)  
624 during post-monsoon from the northwest of the monitoring station is diluted by other sources  
625 (such as vehicular emissions from highways, crop residue burning, and open burning). The  
626 contribution of biofuel burning (which has a higher burning efficiency) during post-monsoon  
627 and winter (Andreae and Merlet, 2001) can also reduce the CO/CO<sub>2</sub> ratios. Figure S4 presents  
628 the wind patterns during the different seasons, revealing the predominant winds from the  
629 northwest during the post-monsoon season. The CO/CO<sub>2</sub> ratios reveal the combined influence  
630 of various sources around and upwind of the monitoring station during the post-monsoon  
631 period.

632 The CH<sub>4</sub>/CO correlation ( $r > 0.7$ ) was stronger during winter than during post-monsoon  
633 across all time windows, suggesting similar sources during winter and different sources during  
634 post-monsoon. The regression slope was higher during winter than during the post-monsoon  
635 period. This was traced to the lack of photosynthetic activity and the dominance of local  
636 emissions and long-range transport. Lin et al. (2015) reported comparable CH<sub>4</sub>/CO ratios at  
637 Pondicherry (PON) and Port Blair (PBL). CH<sub>4</sub> and CO emissions from biomass, biofuel  
638 burning and livestock estimated from EDGAR v4.2, 2011 indicate a CH<sub>4</sub>/CO ratio of 0.64 –  
639 0.69 over the Indian subcontinent from 2000-2008. These ratios are comparable to those  
640 observed during both seasons at Sonipat.

641 In summary, this study demonstrated that this high temporal CO<sub>2</sub> variability across the  
642 IGP region arises from an interplay of local anthropogenic and biomass-burning emissions,  
643 biospheric fluxes, and prevailing meteorology.

644

## 645 **5. Conclusions**

646 In this study, we conducted high frequency measurements of atmospheric CO<sub>2</sub> mole fractions  
647 at a suburban station in the Indo-Gangetic Plain, Sonipat and investigated the carbon cycle  
648 dynamics over IGP. The atmospheric CO<sub>2</sub> mole fractions from February 2023 to January 2025  
649 have been measured using a GHG analyser with laser-based cavity ring-down spectroscopy.  
650 CO<sub>2</sub> molefractions over Sonipat recorded an annual average of  $440.8 \pm 19.7$  parts per million  
651 (ppm) in 2024, with a very high seasonal variability of  $\sim 60$  ppm, much higher than that of other  
652 monitoring stations in the same latitudnal band. Post-monsoon recorded the highest diurnal  
653 variability ( $\sim 60$  ppm) and monsoon recorded the least ( $\sim 20$  ppm) with a consistent diurnal  
654 pattern irrespective of season. By examining a series of observational and modelling data, such  
655 as ground-based and satellite-based measurements, three model outputs, ecosystem proxy  
656 variables, and the tracer-tracer analysis technique, we identified the drivers of the high temporal  
657 variability of CO<sub>2</sub> over Sonipat and the IGP region. First, this high seasonality is attributed to  
658 elevated CO<sub>2</sub> mole fractions in November (post-monsoon), driven by local emissions and crop  
659 residue burning. We found that biospheric activity was the primary driver of seasonal changes  
660 over Sonipat, with anthropogenic emissions and soil respiration as the major sources and  
661 photosynthetic carbon uptake as the major sink. In addition, boundary-layer dynamics and air-  
662 mass transport from upwind regions significantly contribute to the buildup of CO<sub>2</sub> mole  
663 fraction. Second, we found that although both the CarbonTracker and MIROC-ACTM models  
664 captured the broad seasonal pattern of CO<sub>2</sub> mole fractions, they substantially underestimated  
665 it. Moreover, the OCO-2 and OCO-3 satellite XCO<sub>2</sub> retrievals also showed similar seasonal

666 variability; however, the satellites could not capture CO<sub>2</sub> enhancements from local sources.  
667 Third, we found that the atmospheric CO<sub>2</sub> mole fraction at Sonipat exhibits a consistent diurnal  
668 pattern irrespective of season, with a maximum during the morning hours, attributed to the  
669 fumigation effect, followed by a gradual decrease during the day and a minimum during the  
670 afternoon hours, when photosynthetic activity is enhanced. Finally, tracer-tracer relationships  
671 across different time periods in the post-monsoon and winter seasons revealed common sources  
672 of CO<sub>2</sub> and CH<sub>4</sub>. The CO/CO<sub>2</sub> ratios reveal the combined influence of vehicular emissions,  
673 crop residue burning, and open burning on CO<sub>2</sub> mole fractions in Sonipat during the post-  
674 monsoon period. This study identified key sources and drivers of the high CO<sub>2</sub> temporal  
675 variability in a data-sparse IGP region. These findings advance our understanding of carbon  
676 cycle dynamics, with direct implications for mitigation and policy.

### 677 **Data availability**

- 678 ● The observational datasets used in this study are publicly available in a Zenodo  
679 archive and can be accessed from [10.5281/zenodo.19628722](https://zenodo.org/record/19628722)
- 680 ● The OCO-2 and OCO-3 data is downloaded from <https://disc.gsfc.nasa.gov/datasets/>.  
681 This study utilizes the bias-corrected OCO-2 v11.1r data product  
682 ([https://disc.gsfc.nasa.gov/datasets/OCO2\\_L2\\_Lite\\_FP\\_11.1r/summary?keywords=oco](https://disc.gsfc.nasa.gov/datasets/OCO2_L2_Lite_FP_11.1r/summary?keywords=oco2)  
683 [o2](https://disc.gsfc.nasa.gov/datasets/OCO2_L2_Lite_FP_11.1r/summary?keywords=oco2)) and the OCO-3 v10.4r data product  
684 ([https://disc.gsfc.nasa.gov/datasets/OCO3\\_L2\\_Lite\\_FP\\_10.4r/summary?keywords=oco](https://disc.gsfc.nasa.gov/datasets/OCO3_L2_Lite_FP_10.4r/summary?keywords=oco3)  
685 [o3](https://disc.gsfc.nasa.gov/datasets/OCO3_L2_Lite_FP_10.4r/summary?keywords=oco3)).
- 686 ● The CT-2020 model outputs were downloaded from  
687 <https://gml.noaa.gov/aftp/products/carbontracker/co2/>. The CASA model outputs  
688 were downloaded from  
689 [https://disc.gsfc.nasa.gov/datasets/GEOS\\_CASAGFED\\_M\\_FLUX\\_3/summary?keyw](https://disc.gsfc.nasa.gov/datasets/GEOS_CASAGFED_M_FLUX_3/summary?keywords=CASA)  
690 [ords=CASA](https://disc.gsfc.nasa.gov/datasets/GEOS_CASAGFED_M_FLUX_3/summary?keywords=CASA).
- 691 ● The ERA5 reanalysis datasets were downloaded from  
692 <https://cds.climate.copernicus.eu/cdsapp#!/dataset/reanalysis-era5-single-levels>.
- 693 ● The satellite estimates of NDVI were downloaded from  
694 <https://www.ncei.noaa.gov/data/land-normalized-difference-vegetation-index/access/>.
- 695 ● This study utilises bias-corrected SIF data from OCO-2 v11r data product  
696 ([https://disc.gsfc.nasa.gov/datasets/OCO2\\_L2\\_Lite\\_SIF\\_11r/summary?keywords=oco](https://disc.gsfc.nasa.gov/datasets/OCO2_L2_Lite_SIF_11r/summary?keywords=oco2%20sif)  
697 [2%20sif](https://disc.gsfc.nasa.gov/datasets/OCO2_L2_Lite_SIF_11r/summary?keywords=oco2%20sif)).

698       • The FluxSat data is downloaded from  
699           [https://avdc.gsfc.nasa.gov/pub/tmp/FluxSat\\_GPP/](https://avdc.gsfc.nasa.gov/pub/tmp/FluxSat_GPP/). This study uses FluxSat version  
700           2.2 dataproduct.

701       • The ObsPack data is available at <https://gml.noaa.gov/ccgg/obspack/data.php>. This  
702           study used ObsPack V2.0 dataproduct.

703

#### 704 **Acknowledgements:**

705 We acknowledge the institutional support and funding from IIT Delhi and other stakeholders  
706 in developing the IIT Delhi Atmospheric Observatory at Sonipat. In particular, we thank  
707 Shahzad Gani (IIT Delhi) for his contribution to the observatory. The CUPI-G operation is  
708 partly supported by the Research Institute for Humanity and Nature (RIHN: a constituent  
709 member of NIHU) Project No. 14200133 (Aakash). We acknowledge the OCO-2, OCO-3,  
710 CASA, CarbonTracker, and ERA5 teams for providing the data used in this study.

711

712

#### 713 **Author Contributions:**

714 **Conceptualization:** VJV, RKK, SP

715 **Data curation:** VJV, RKK, JR, DG, SD, TN, YM, PKP

716 **Investigation, Methodology:** VJV, RKK, SP, PKP

717 **Software, Visualisation:** VJV

718 **Writing – original draft:** VJV

719 **Writing – review & editing:** RKK, SP, JR, DG, SD, YM, PKP

720

#### 721 **Competing interests**

722 The authors declare that they have no conflict of interest.

723 **References**

- 724 Aburas, M. M., Abdullah, S. H., Ramli, M. F., and Ash'aari, Z. H.: Measuring Land Cover  
725 Change in Seremban, Malaysia Using NDVI Index, *Procedia Environmental Sciences*, 30,  
726 238–243, <https://doi.org/10.1016/j.proenv.2015.10.043>, 2015.
- 727 Ammoura, L., Xueref-Remy, I., Gros, V., Baudic, A., Bonsang, B., Petit, J.-E., Perrussel, O.,  
728 Bonnaire, N., Sciare, J., and Chevallier, F.: Atmospheric measurements of ratios between  
729 CO<sub>2</sub> and co-emitted species from traffic: a tunnel study in the Paris  
730 megacity, *Atmos. Chem. Phys.*, 14, 12871–12882, [https://doi.org/10.5194/acp-14-12871-](https://doi.org/10.5194/acp-14-12871-2014)  
731 2014, 2014.
- 732 Andreae, M. O. and Merlet, P.: Emission of trace gases and aerosols from biomass burning,  
733 *Global Biogeochemical Cycles*, 15, 955–966, <https://doi.org/10.1029/2000GB001382>, 2001.
- 734 Apadula, F., Cassardo, C., Ferrarese, S., Heltai, D., and Lanza, A.: Thirty Years of  
735 Atmospheric CO<sub>2</sub> Observations at the Plateau Rosa Station, Italy, *Atmosphere*, 10, 418,  
736 <https://doi.org/10.3390/atmos10070418>, 2019.
- 737 Baars, H., Ansmann, A., Engelmann, R., and Althausen, D.: Continuous monitoring of the  
738 boundary-layer top with lidar, *Atmospheric Chemistry and Physics*, 8, 7281–7296,  
739 <https://doi.org/10.5194/acp-8-7281-2008>, 2008.
- 740 Baker, A. K., Schuck, T. J., Brenninkmeijer, C. A. M., Rauthe-Schöch, A., Slemr, F., van  
741 Velthoven, P. F. J., and Lelieveld, J.: Estimating the contribution of monsoon-related  
742 biogenic production to methane emissions from South Asia using CARIBIC observations,  
743 *Geophysical Research Letters*, 39, <https://doi.org/10.1029/2012GL051756>, 2012.
- 744 Bakwin, P. S., Tans, P. S., Zhao, C., Ussler III, W., and Quesnell, E.: Measurements of  
745 carbon dioxide on a very tall tower, *Tellus B: Chemical and Physical Meteorology*, 47, 535–  
746 549, <https://doi.org/10.3402/tellusb.v47i5.16070>, 1995.
- 747 Bhattacharya, S. K., Borole, D. V., Franczy, R. J., Allison, C. E., Steele, L. P., Krummel, P.,  
748 Langenfelds, R., Masarie, K. A., Tiwari, Y. K., and Patra, P. K.: Trace gases and CO<sub>2</sub> isotope  
749 records from Cabo de Rama, India, *Current Science*, 97, 1336–1344, 2009.
- 750 Bisht, J. S. H., Machida, T., Chandra, N., Tsuboi, K., Patra, P. K., Umezawa, T., Niwa, Y.,  
751 Sawa, Y., Morimoto, S., Nakazawa, T., Saitoh, N., and Takigawa, M.: Seasonal Variations of  
752 SF<sub>6</sub>, CO<sub>2</sub>, CH<sub>4</sub>, and N<sub>2</sub>O in the UT/LS Region due to Emissions, Transport, and Chemistry,  
753 *JGR Atmospheres*, 126, e2020JD033541, <https://doi.org/10.1029/2020JD033541>, 2021.
- 754 Brad Weir (2024), MiCASA Daily NPP Rh Fire Fuel Fluxes 0.1 degree × 0.1 degree V1,  
755 Greenbelt, MD, USA, NASA Center for Climate Simulation (NCCS) DataPortal, Accessed:  
756 [March 20, 2025], 10.5067/ZBXSA1LEN453
- 757 Byrne, B., Jones, D. B. A., Strong, K., Zeng, Z. -C., Deng, F., and Liu, J.: Sensitivity of CO<sub>2</sub>  
758 surface flux constraints to observational coverage, *JGR Atmospheres*, 122, 6672–6694,  
759 <https://doi.org/10.1002/2016JD026164>, 2017.
- 760 Chakraborty, S., Tiwari, Y. K., Deb Burman, P. K., Baidya Roy, S., and Valsala, V.:  
761 Observations and Modeling of GHG Concentrations and Fluxes Over India, in: Assessment

762 of Climate Change over the Indian Region: A Report of the Ministry of Earth Sciences  
763 (MoES), Government of India, edited by: Krishnan, R., Sanjay, J., Gnanaseelan, C.,  
764 Mujumdar, M., Kulkarni, A., and Chakraborty, S., Springer, Singapore, 73–92,  
765 [https://doi.org/10.1007/978-981-15-4327-2\\_4](https://doi.org/10.1007/978-981-15-4327-2_4), 2020.

766 Chandra, N., Lal, S., Venkataramani, S., Patra, P. K., and Sheel, V.: Temporal variations of  
767 atmospheric CO<sub>2</sub> and CO at Ahmedabad in western India, *Atmos.*  
768 *Chem. Phys.*, 16, 6153–6173, <https://doi.org/10.5194/acp-16-6153-2016>, 2016.

769 Chandra, N., Venkataramani, S., Lal, S., Patra, P. K., Ramonet, M., Lin, X., and Sharma, S.  
770 K.: Observational evidence of high methane emissions over a city in western India,  
771 *Atmospheric Environment*, 202, 41–52, <https://doi.org/10.1016/j.atmosenv.2019.01.007>,  
772 2019.

773 Chandra, N., Patra, P. K., Bisht, J. S. H., Ito, A., Umezawa, T., Saigusa, N., Morimoto, S.,  
774 Aoki, S., Janssens-Maenhout, G., Fujita, R., Takigawa, M., Watanabe, S., Saitoh, N., and  
775 Canadell, J. G.: Emissions from the Oil and Gas Sectors, Coal Mining and Ruminant Farming  
776 Drive Methane Growth over the Past Three Decades, *Journal of the Meteorological Society*  
777 *of Japan*, 99, 309–337, <https://doi.org/10.2151/jmsj.2021-015>, 2021.

778 Chandra, N., Patra, P. K., Niwa, Y., Ito, A., Iida, Y., Goto, D., Morimoto, S., Kondo, M.,  
779 Takigawa, M., Hajima, T., and Watanabe, M.: Estimated regional CO<sub>2</sub> flux and uncertainty  
780 based on an ensemble of atmospheric CO<sub>2</sub> inversions, *Atmos. Chem. Phys.*, 22, 9215–9243,  
781 <https://doi.org/10.5194/acp-22-9215-2022>, 2022.

782 Chen, H., Karion, A., Rella, C. W., Winderlich, J., Gerbig, C., Filges, A., Newberger, T.,  
783 Sweeney, C., and Tans, P. P.: Accurate measurements of carbon monoxide in humid air using  
784 the cavity ring-down spectroscopy (CRDS) technique, *Atmospheric Measurement*  
785 *Techniques*, 6, 1031–1040, <https://doi.org/10.5194/amt-6-1031-2013>, 2013.

786 Chen, Y., Hall, J., Van Wees, D., Andela, N., Hantson, S., Giglio, L., Van Der Werf, G. R.,  
787 Morton, D. C., and Randerson, J. T.: Multi-decadal trends and variability in burned area from  
788 the fifth version of the Global Fire Emissions Database (GFED5), *Earth Syst. Sci. Data*, 15,  
789 5227–5259, <https://doi.org/10.5194/essd-15-5227-2023>, 2023.

790 Crisp, D., Pollock, H. R., Rosenberg, R., Chapsky, L., Lee, R. A. M., Oyafuso, F. A.,  
791 Frankenberg, C., O'Dell, C. W., Bruegge, C. J., Doran, G. B., Eldering, A., Fisher, B. M., Fu,  
792 D., Gunson, M. R., Mandrake, L., Osterman, G. B., Schwandner, F. M., Sun, K., Taylor, T.  
793 E., Wennberg, P. O., and Wunch, D.: The on-orbit performance of the Orbiting Carbon  
794 Observatory-2 (OCO-2) instrument and its radiometrically calibrated products, *Atmos. Meas.*  
795 *Tech.*, 10, 59–81, <https://doi.org/10.5194/amt-10-59-2017>, 2017.

796 Das, C., Kunchala, R. K., Chandra, N., Chhabra, A., and Pandya, M. R.: Characterizing the  
797 regional XCO<sub>2</sub> variability and its association with ENSO over India inferred from GOSAT  
798 and OCO-2 satellite observations, *Science of The Total Environment*, 902, 166176,  
799 <https://doi.org/10.1016/j.scitotenv.2023.166176>, 2023.

800 Eldering, A., O'Dell, C. W., Wennberg, P. O., Crisp, D., Gunson, M. R., Viatte, C., Avis, C.,  
801 Braverman, A., Castano, R., Chang, A., Chapsky, L., Cheng, C., Connor, B., Dang, L.,  
802 Doran, G., Fisher, B., Frankenberg, C., Fu, D., Granat, R., Hobbs, J., Lee, R. A. M.,  
803 Mandrake, L., McDuffie, J., Miller, C. E., Myers, V., Natraj, V., O'Brien, D., Osterman, G.

- 804 B., Oyafuso, F., Payne, V. H., Pollock, H. R., Polonsky, I., Roehl, C. M., Rosenberg, R.,  
805 Schwandner, F., Smyth, M., Tang, V., Taylor, T. E., To, C., Wunch, D., and Yoshimizu, J.:  
806 The Orbiting Carbon Observatory-2: first 18 months of science data products, *Atmos. Meas.*  
807 *Tech.*, 10, 549–563, <https://doi.org/10.5194/amt-10-549-2017>, 2017.
- 808 Eldering, A., Taylor, T. E., O’Dell, C. W., and Pavlick, R.: The OCO-3 mission:  
809 measurement objectives and expected performance based on 1 year of simulated data, *Atmos.*  
810 *Meas. Tech.*, 12, 2341–2370, <https://doi.org/10.5194/amt-12-2341-2019>, 2019.
- 811 Fan, N., & Forkel, M. (2025). Drivers of the enhanced amplitude of atmospheric CO<sub>2</sub> in  
812 northern terrestrial ecosystems. <https://doi.org/10.5194/egusphere-egu25-7279>
- 813 Fang, S. X., Tans, P. P., Steinbacher, M., Zhou, L. X., and Luan, T.: Comparison of the  
814 regional CO<sub>2</sub> mole fraction filtering approaches at a WMO/GAW regional station in China,  
815 *Atmospheric Measurement Techniques*, 8, 5301–5313, [https://doi.org/10.5194/amt-8-5301-](https://doi.org/10.5194/amt-8-5301-2015)  
816 2015, 2015.
- 817 Fawzy, S., Osman, A. I., Doran, J., and Rooney, D. W.: Strategies for mitigation of climate  
818 change: a review, *Environ Chem Lett*, 18, 2069–2094, [https://doi.org/10.1007/s10311-020-](https://doi.org/10.1007/s10311-020-01059-w)  
819 01059-w, 2020.
- 820 Frankenberg, C., O’Dell, C., Berry, J., Guanter, L., Joiner, J., Köhler, P., Pollock, R., and  
821 Taylor, T. E.: Prospects for chlorophyll fluorescence remote sensing from the Orbiting  
822 Carbon Observatory-2, *Remote Sensing of Environment*, 147, 1–12,  
823 <https://doi.org/10.1016/j.rse.2014.02.007>, 2014.
- 824 Friedlingstein, P., O’Sullivan, M., Jones, M. W., Andrew, R. M., Hauck, J., Landschützer, P.,  
825 Le Quéré, C., Li, H., Luijkx, I. T., Olsen, A., Peters, G. P., Peters, W., Pongratz, J.,  
826 Schwingshackl, C., Sitch, S., Canadell, J. G., Ciais, P., Jackson, R. B., Alin, S. R., Arneth, A.,  
827 Arora, V., Bates, N. R., Becker, M., Bellouin, N., Berghoff, C. F., Bittig, H. C., Bopp, L.,  
828 Cadule, P., Campbell, K., Chamberlain, M. A., Chandra, N., Chevallier, F., Chini, L. P.,  
829 Colligan, T., Decayeux, J., Djutchouang, L. M., Dou, X., Duran Rojas, C., Enyo, K., Evans,  
830 W., Fay, A. R., Feely, R. A., Ford, D. J., Foster, A., Gasser, T., Gehlen, M., Gkritzalis, T.,  
831 Grassi, G., Gregor, L., Gruber, N., Gürses, Ö., Harris, I., Hefner, M., Heinke, J., Hurtt, G. C.,  
832 Iida, Y., Ilyina, T., Jacobson, A. R., Jain, A. K., Jarníková, T., Jersild, A., Jiang, F., Jin, Z.,  
833 Kato, E., Keeling, R. F., Klein Goldewijk, K., Knauer, J., Korsbakken, J. I., Lan, X., Lauvset,  
834 S. K., Lefèvre, N., Liu, Z., Liu, J., Ma, L., Maksyutov, S., Marland, G., Mayot, N., McGuire,  
835 P. C., Metzl, N., Monacci, N. M., Morgan, E. J., Nakaoka, S.-I., Neill, C., Niwa, Y., Nützel,  
836 T., Olivier, L., Ono, T., Palmer, P. I., Pierrot, D., Qin, Z., Resplandy, L., Roobaert, A.,  
837 Rosan, T. M., Rödenbeck, C., Schwinger, J., Smallman, T. L., Smith, S. M., Sospedra-  
838 Alfonso, R., Steinhoff, T., et al.: Global Carbon Budget 2024, *Earth Syst. Sci. Data*, 17, 965–  
839 1039, <https://doi.org/10.5194/essd-17-965-2025>, 2025.
- 840 Halder, S., Tiwari, Y. K., Valsala, V., Sreeush, M. G., Sijikumar, S., Janardanan, R., &  
841 Maksyutov, S. (2021). Quantification of enhancement in atmospheric CO<sub>2</sub> background due to  
842 Indian biospheric fluxes and fossil fuel emissions. *Journal of Geophysical Research:*  
843 *Atmospheres*, 126(13), e2021JD034545.
- 844 Harriss, R. C., Sachse, G. W., Collins Jr., J. E., Wade, L., Bartlett, K. B., Talbot, R. W.,  
845 Browell, E. V., Barrie, L. A., Hill, G. F., and Burney, L. G.: Carbon monoxide and methane

- 846 over Canada: July–August 1990, *Journal of Geophysical Research: Atmospheres*, 99, 1659–  
847 1669, <https://doi.org/10.1029/93JD01906>, 1994.
- 848 Huang, J., Golombek, A., Prinn, R., Weiss, R., Fraser, P., Simmonds, P., Dlugokencky, E. J.,  
849 Hall, B., Elkins, J., Steele, P., Langenfelds, R., Krummel, P., Dutton, G., and Porter, L.:  
850 Estimation of regional emissions of nitrous oxide from 1997 to 2005 using multinetwork  
851 measurements, a chemical transport model, and an inverse method, *Journal of Geophysical*  
852 *Research: Atmospheres*, 113, <https://doi.org/10.1029/2007JD009381>, 2008.
- 853 Huang, J., Yu, H., Guan, X., Wang, G., and Guo, R.: Accelerated dryland expansion under  
854 climate change, *Nature Clim Change*, 6, 166–171, <https://doi.org/10.1038/nclimate2837>,  
855 2016.
- 856 IPCC, 2021: *Climate Change 2021: The Physical Science Basis. Contribution of Working*  
857 *Group I to the Sixth Assessment Report of the Intergovernmental Panel on Climate*  
858 *Change*[Masson-Delmotte, V., P. Zhai, A. Pirani, S.L. Connors, C. Péan, S. Berger, N. Caud,  
859 Y. Chen, L. Goldfarb, M.I. Gomis, M. Huang, K. Leitzell, E. Lonnoy, J.B.R. Matthews, T.K.  
860 Maycock, T. Waterfield, O. Yelekçi, R. Yu, and B. Zhou (eds.)]. Cambridge University  
861 Press, Cambridge, United Kingdom and New York, NY, USA, In press,  
862 doi:10.1017/9781009157896.
- 863 Ito, A.: Disequilibrium of terrestrial ecosystem CO<sub>2</sub> budget caused by disturbance-induced  
864 emissions and non-CO<sub>2</sub> carbon export flows: a global model assessment, *Earth Syst. Dynam.*,  
865 10, 685–709, <https://doi.org/10.5194/esd-10-685-2019>, 2019.
- 866 Jain, C. D., Singh, V., Akhil Raj, S. T., Madhavan, B. L., and Ratnam, M. V.: Local emission  
867 and long-range transport impacts on the CO, CO<sub>2</sub>, and CH<sub>4</sub> concentrations at a tropical rural  
868 site, *Atmospheric Environment*, 254, 118397,  
869 <https://doi.org/10.1016/j.atmosenv.2021.118397>, 2021.
- 870 Jing, X., Huang, J., Wang, G., Higuchi, K., Bi, J., Sun, Y., Yu, H., and Wang, T.: The effects  
871 of clouds and aerosols on net ecosystem CO<sub>2</sub> exchange over semi-arid Loess Plateau of  
872 Northwest China, *Atmospheric Chemistry and Physics*, 10, 8205–8218,  
873 <https://doi.org/10.5194/acp-10-8205-2010>, 2010.
- 874 Joiner, J. and Yoshida, Y.: Satellite-based reflectances capture large fraction of variability in  
875 global gross primary production (GPP) at weekly time scales, *Agricultural and Forest*  
876 *Meteorology*, 291, 108092, <https://doi.org/10.1016/j.agrformet.2020.108092>, 2020.
- 877 Joiner, J., Yoshida, Y., Zhang, Y., Duveiller, G., Jung, M., Lyapustin, A., Wang, Y., and  
878 Tucker, C. J.: Estimation of Terrestrial Global Gross Primary Production (GPP) with Satellite  
879 Data-Driven Models and Eddy Covariance Flux Data, *Remote Sensing*, 10, 1346,  
880 <https://doi.org/10.3390/rs10091346>, 2018.
- 881 Jones, M. W., Andrew, R. M., Peters, G. P., Janssens-Maenhout, G., De-Gol, A. J., Ciais, P.,  
882 Patra, P. K., Chevallier, F., and Le Quéré, C.: Gridded fossil CO<sub>2</sub> emissions and related O<sub>2</sub>  
883 combustion consistent with national inventories 1959–2018, *Sci Data*, 8, 2,  
884 <https://doi.org/10.1038/s41597-020-00779-6>, 2021.
- 885 Kar, J., Bremer, H., Drummond, J. R., Rochon, Y. J., Jones, D. B. A., Nichitiu, F., Zou, J.,  
886 Liu, J., Gille, J. C., Edwards, D. P., Deeter, M. N., Francis, G., Ziskin, D., and Warner, J.:

887 Evidence of vertical transport of carbon monoxide from Measurements of Pollution in the  
888 Troposphere (MOPITT), *Geophysical Research Letters*, 31,  
889 <https://doi.org/10.1029/2004GL021128>, 2004.

890 Krishnapriya, M., Pattanaik, D. R., Kumar, A., Ramana, M. V., & Naidu, C. V. (2025).  
891 Spatio-temporal dynamics of atmospheric CO<sub>2</sub> over India and its inter-relationship with  
892 combustion emissions, ecosystem exchange, and meteorological factors: M Krishnapriya et  
893 al. *Journal of Earth System Science*, 134(4), 193.

894 Krol, M., Houweling, S., Bregman, B., van den Broek, M., Segers, A., van Velthoven, P.,  
895 Peters, W., Dentener, F., and Bergamaschi, P.: The two-way nested global chemistry-  
896 transport zoom model TM5: algorithm and applications, *Atmospheric Chemistry and Physics*  
897 *Discussions*, 4, 3975–4018, 2004.

898 Kumar, A., Yu, Z.-G., Klemeš, J. J., and Bokhari, A.: A state-of-the-art review of greenhouse  
899 gas emissions from Indian hydropower reservoirs, *Journal of Cleaner Production*, 320,  
900 128806, <https://doi.org/10.1016/j.jclepro.2021.128806>, 2021.

901 Kunchala, R. K., Girach, I., Das, C., Jain, C., Burman, P. K. D., Pathakoti, M., ... & Jain, V.  
902 (2025). Carbon dioxide (CO<sub>2</sub>) variations across India: Synthesis of observations and model  
903 simulations. *Atmospheric Environment*, 121746.

904 Kunchala, R. K., Patra, P. K., Kumar, K. N., Chandra, N., Attada, R., and Karumuri, R. K.:  
905 Spatio-temporal variability of XCO<sub>2</sub> over Indian region inferred from Orbiting Carbon  
906 Observatory (OCO-2) satellite and Chemistry Transport Model, *Atmospheric Research*, 269,  
907 106044, <https://doi.org/10.1016/j.atmosres.2022.106044>, 2022.

908 Kuttippurath, J., Peter, R., Singh, A., and Raj, S.: The increasing atmospheric CO<sub>2</sub> over  
909 India: Comparison to global trends, *iScience*, 25, 104863,  
910 <https://doi.org/10.1016/j.isci.2022.104863>, 2022.

911 Lai, S. C., Baker, A. K., Schuck, T. J., van Velthoven, P., Oram, D. E., Zahn, A., Hermann,  
912 M., Weigelt, A., Slemr, F., Brenninkmeijer, C. a. M., and Ziereis, H.: Pollution events  
913 observed during CARIBIC flights in the upper troposphere between South China and the  
914 Philippines, *Atmospheric Chemistry and Physics*, 10, 1649–1660,  
915 <https://doi.org/10.5194/acp-10-1649-2010>, 2010.

916 Le Quéré, C., Andrew, R. M., Friedlingstein, P., Sitch, S., Pongratz, J., Manning, A. C.,  
917 Korsbakken, J. I., Peters, G. P., Canadell, J. G., Jackson, R. B., Boden, T. A., Tans, P. P.,  
918 Andrews, O. D., Arora, V. K., Bakker, D. C. E., Barbero, L., Becker, M., Betts, R. A., Bopp,  
919 L., Chevallier, F., Chini, L. P., Ciais, P., Cosca, C. E., Cross, J., Currie, K., Gasser, T., Harris,  
920 I., Hauck, J., Haverd, V., Houghton, R. A., Hunt, C. W., Hurtt, G., Ilyina, T., Jain, A. K.,  
921 Kato, E., Kautz, M., Keeling, R. F., Klein Goldewijk, K., Körtzinger, A., Landschützer, P.,  
922 Lefèvre, N., Lenton, A., Lienert, S., Lima, I., Lombardozzi, D., Metzl, N., Millero, F.,  
923 Monteiro, P. M. S., Munro, D. R., Nabel, J. E. M. S., Nakaoka, S., Nojiri, Y., Padin, X. A.,  
924 Peregón, A., Pfeil, B., Pierrot, D., Poulter, B., Rehder, G., Reimer, J., Rödenbeck, C.,  
925 Schwinger, J., Séférian, R., Skjelvan, I., Stocker, B. D., Tian, H., Tilbrook, B., Tubiello, F.  
926 N., Van Der Laan-Luijkx, I. T., Van Der Werf, G. R., Van Heuven, S., Viovy, N., Vuichard,  
927 N., Walker, A. P., Watson, A. J., Wiltshire, A. J., Zaehle, S., and Zhu, D.: Global Carbon  
928 Budget 2017, *Earth Syst. Sci. Data*, 10, 405–448, <https://doi.org/10.5194/essd-10-405-2018>,  
929 2018.

- 930 ICOS RI, 2020. ICOS Atmosphere Station Specifications V2.0 (editor: O. Laurent). ICOS  
931 ERIC. <https://doi.org/10.18160/GK28-2188>  
932
- 933 Lin, X., Indira, N. K., Ramonet, M., Delmotte, M., Ciais, P., Bhatt, B. C., Reddy, M. V.,  
934 Anghuk, D., Balakrishnan, S., Jorphail, S., Dorjai, T., Mahey, T. T., Patnaik, S., Begum, M.,  
935 Brenninkmeijer, C., Durairaj, S., Kirubakaran, R., Schmidt, M., Swathi, P. S., Vinithkumar,  
936 N. V., Yver Kwok, C., and Gaur, V. K.: Long-lived atmospheric trace gases measurements in  
937 flask samples from three stations in India, *Atmos. Chem. Phys.*, 15, 9819–9849,  
938 <https://doi.org/10.5194/acp-15-9819-2015>, 2015.
- 939 Lin, X., Ciais, P., Bousquet, P., Ramonet, M., Yin, Y., Balkanski, Y., Cozic, A., Delmotte,  
940 M., Evangeliou, N., Indira, N. K., Locatelli, R., Peng, S., Piao, S., Saunois, M., Swathi, P. S.,  
941 Wang, R., Yver-Kwok, C., Tiwari, Y. K., and Zhou, L.: Simulating CH<sub>4</sub> and CO<sub>2</sub> over South  
942 and East Asia using the zoomed chemistry transport model LMDz-INCA, *Atmos. Chem.*  
943 *Phys.*, 18, 9475–9497, <https://doi.org/10.5194/acp-18-9475-2018>, 2018.
- 944 Liu, J., Bowman, K. W., Lee, M., Henze, D. K., Bousserez, N., Brix, H., Collatz, G. J.,  
945 Menemenlis, D., Ott, L., Pawson, S., Jones, D., and Nassar, R.: Carbon monitoring system  
946 flux estimation and attribution: impact of ACOS-GOSAT XCO<sub>2</sub> sampling on the inference of  
947 terrestrial biospheric sources and sinks, *Tellus B: Chemical and Physical Meteorology*, 66,  
948 22486, <https://doi.org/10.3402/tellusb.v66.22486>, 2014.
- 949 Lopez, M.: Estimation des émissions de gaz à effet de serre à différentes échelles en France à  
950 l'aide d'observations de haute précision, phdthesis, Université Paris Sud - Paris XI, 2012.
- 951 Mahesh, P., Sreenivas, G., Rao, P. V. N., Dadhwal, V. K., Sai Krishna, S. V. S., and  
952 Mallikarjun, K.: High-precision surface-level CO<sub>2</sub> and CH<sub>4</sub> using off-axis integrated cavity  
953 output spectroscopy (OA-ICOS) over Shadnagar, India, *International Journal of Remote*  
954 *Sensing*, 36, 5754–5765, <https://doi.org/10.1080/01431161.2015.1104744>, 2015.
- 955 Mangaraj, P., Matsumi, Y., Nakayama, T., Biswal, A., Yamaji, K., Araki, H., ... & Mor, S.  
956 (2025). Weak coupling of observed surface PM<sub>2.5</sub> in Delhi-NCR with rice crop residue  
957 burning in Punjab and Haryana. *Npj Climate and Atmospheric Science*, 8(1), 18.
- 958 Masarie, K. A., Peters, W., Jacobson, A. R., and Tans, P. P.: ObsPack: a framework for the  
959 preparation, delivery, and attribution of atmospheric greenhouse gas measurements, *Earth*  
960 *Syst. Sci. Data*, 6, 375–384, <https://doi.org/10.5194/essd-6-375-2014>, 2014.
- 961 Matsueda, H., Inoue, H. Y., Ishii, M., and Tsutsumi, Y.: Large injection of carbon monoxide  
962 into the upper troposphere due to intense biomass burning in 1997, *J. Geophys. Res.*, 104,  
963 26867–26879, <https://doi.org/10.1029/1999JD900193>, 1999.
- 964 Mauzerall, D. L., Logan, J. A., Jacob, D. J., Anderson, B. E., Blake, D. R., Bradshaw, J. D.,  
965 Heikes, B., Sachse, G. W., Singh, H., and Talbot, B.: Photochemistry in biomass burning  
966 plumes and implications for tropospheric ozone over the tropical South Atlantic, *J. Geophys.*  
967 *Res.*, 103, 8401–8423, <https://doi.org/10.1029/97JD02612>, 1998.
- 968 Metya, A., Datye, A., Chakraborty, S., Tiwari, Y. K., Sarma, D., Bora, A., and Gogoi, N.:  
969 Diurnal and seasonal variability of CO<sub>2</sub> and CH<sub>4</sub> concentration in a semi-urban environment  
970 of western India, *Sci Rep*, 11, 2931, <https://doi.org/10.1038/s41598-021-82321-1>, 2021.

- 971 Mühle, J., Brenninkmeijer, C. a. M., Rhee, T. S., Slemr, F., Oram, D. E., Penkett, S. A., and  
972 Zahn, A.: Biomass burning and fossil fuel signatures in the upper troposphere observed  
973 during a CARIBIC flight from Namibia to Germany, *Geophysical Research Letters*, 29, 16-1-  
974 16-4, <https://doi.org/10.1029/2002GL015764>, 2002.
- 975 Munksgaard, N. C., Lee, I. L., Napier, T. P., Zwart, C., Cernusak, L. A., & Bird, M. I. (2022).  
976 One year of spectroscopic high-frequency measurements of atmospheric CO<sub>2</sub>, CH<sub>4</sub>, H.  
977 *Geoscience Data Journal*. <https://doi.org/10.1002/gdj3.180>
- 978 Nalini, K., Sijikumar, S., Valsala, V., Tiwari, Y. K., and Ramachandran, R.: Designing  
979 surface CO<sub>2</sub> monitoring network to constrain the Indian land fluxes, *Atmospheric*  
980 *Environment*, 218, 117003, <https://doi.org/10.1016/j.atmosenv.2019.117003>, 2019.
- 981 Nath, B.: Quantitative Assessment of Forest Cover Change of a Part of Bandarban Hill Tracts  
982 Using NDVI Techniques, *Journal of Geosciences and Geomatics*, 2, 21–27,  
983 <https://doi.org/10.12691/jgg-2-1-4>, 2014.
- 984 Nishanth, T., Praseed, K. M., Kumar, M. K. S., and Valsaraj, K. T.: Observational Study of  
985 Surface O<sub>3</sub>, NO<sub>x</sub>, CH<sub>4</sub> and Total NMHCs at Kannur, India, *Aerosol Air Qual. Res.*, 14,  
986 1074–1088, <https://doi.org/10.4209/aaqr.2012.11.0323>, 2014.
- 987 Niwa, Y., Machida, T., Sawa, Y., Matsueda, H., Schuck, T. J., Brenninkmeijer, C. A. M.,  
988 Imasu, R., and Satoh, M.: Imposing strong constraints on tropical terrestrial CO<sub>2</sub> fluxes using  
989 passenger aircraft based measurements, *Journal of Geophysical Research: Atmospheres*, 117,  
990 <https://doi.org/10.1029/2012JD017474>, 2012.
- 991 Nomura, S., Naja, M., Ahmed, M. K., Mukai, H., Terao, Y., Machida, T., Sasakawa, M., and  
992 Patra, P. K.: Measurement report: Regional characteristics of seasonal and long-term  
993 variations in greenhouse gases at Nainital, India, and Comilla, Bangladesh, *Atmos. Chem.*  
994 *Phys.*, 21, 16427–16452, <https://doi.org/10.5194/acp-21-16427-2021>, 2021.
- 995 Paris, J.-D., Ciais, P., Nédélec, P., Ramonet, M., Belan, B. D., Arshinov, M. Yu., Golitsyn, G.  
996 S., Granberg, I., Stohl, A., Cayez, G., Athier, G., Boumard, F., and Cousin, J.-M.: The YAK-  
997 AEROSIB transcontinental aircraft campaigns: new insights on the transport of CO<sub>2</sub>, CO and  
998 O<sub>3</sub> across Siberia, *Tellus B: Chemical and Physical Meteorology*, 60, 551–568,  
999 <https://doi.org/10.1111/j.1600-0889.2008.00369.x>, 2008.
- 1000 Park, M., Randel, W. J., Emmons, L. K., and Livesey, N. J.: Transport pathways of carbon  
1001 monoxide in the Asian summer monsoon diagnosed from Model of Ozone and Related  
1002 Tracers (MOZART), *J. Geophys. Res.*, 114, 2008JD010621,  
1003 <https://doi.org/10.1029/2008JD010621>, 2009.
- 1004 Pathakoti, M., D.V., M., Gaddamidi, S., Arun, S. S., Bothale, R. V., Chauhan, P., P, R., K.S.,  
1005 R., and Chandra, N.: Three-dimensional view of CO<sub>2</sub> variability in the atmosphere over the  
1006 Indian region, *Atmospheric Research*, 290, 106785,  
1007 <https://doi.org/10.1016/j.atmosres.2023.106785>, 2023.
- 1008 Patil, M. N., Dharmaraj, T., Waghmare, R. T., Prabha, T. V., and Kulkarni, J. R.:  
1009 Measurements of carbon dioxide and heat fluxes during monsoon-2011 season over rural site  
1010 of India by eddy covariance technique, *J Earth Syst Sci*, 123, 177–185,  
1011 <https://doi.org/10.1007/s12040-013-0374-z>, 2014.

- 1012 Patra, P. K., Niwa, Y., Schuck, T. J., Brenninkmeijer, C. a. M., Machida, T., Matsueda, H.,  
1013 and Sawa, Y.: Carbon balance of South Asia constrained by passenger aircraft CO<sub>2</sub>  
1014 measurements, *Atmospheric Chemistry and Physics*, 11, 4163–4175,  
1015 <https://doi.org/10.5194/acp-11-4163-2011>, 2011.
- 1016 Patra, P. K., Canadell, J. G., Houghton, R. A., Piao, S. L., Oh, N.-H., Ciais, P., Manjunath, K.  
1017 R., Chhabra, A., Wang, T., Bhattacharya, T., Bousquet, P., Hartman, J., Ito, A., Mayorga, E.,  
1018 Niwa, Y., Raymond, P. A., Sarma, V. V. S. S., and Lasco, R.: The carbon budget of South  
1019 Asia, *Biogeosciences*, 10, 513–527, <https://doi.org/10.5194/bg-10-513-2013>, 2013.
- 1020 Patra, P. K., Crisp, D., Kaiser, J. W., Wunch, D., Saeki, T., Ichii, K., Sekiya, T., Wennberg,  
1021 P. O., Feist, D. G., Pollard, D. F., Griffith, D. W. T., Velasco, V. A., De Maziere, M., Sha, M.  
1022 K., Roehl, C., Chatterjee, A., and Ishijima, K.: The Orbiting Carbon Observatory (OCO-2)  
1023 tracks 2–3 peta-gram increase in carbon release to the atmosphere during the 2014–2016 El  
1024 Niño, *Sci Rep*, 7, 13567, <https://doi.org/10.1038/s41598-017-13459-0>, 2017.
- 1025 Patra, P. K., Takigawa, M., Watanabe, S., Chandra, N., Ishijima, K., and Yamashita, Y.:  
1026 Improved Chemical Tracer Simulation by MIROC4.0-based Atmospheric Chemistry-  
1027 Transport Model (MIROC4-ACTM), *Sola*, 14, 91–96, <https://doi.org/10.2151/sola.2018-016>,  
1028 2018.
- 1029 Peters, W., Miller, J. B., Whitaker, J., Denning, A. S., Hirsch, A., Krol, M. C., Zupanski, D.,  
1030 Bruhwiler, L., and Tans, P. P.: An ensemble data assimilation system to estimate CO<sub>2</sub> surface  
1031 fluxes from atmospheric trace gas observations, *Journal of Geophysical Research:*  
1032 *Atmospheres*, 110, <https://doi.org/10.1029/2005JD006157>, 2005.
- 1033 Philip, S., Johnson, M. S., Potter, C., Genovesse, V., Baker, D. F., Haynes, K. D., Henze, D.  
1034 K., Liu, J., and Poulter, B.: Prior biosphere model impact on global terrestrial CO<sub>2</sub> fluxes  
1035 estimated from OCO-2 retrievals, *Atmos. Chem. Phys.*, 19, 13267–13287,  
1036 <https://doi.org/10.5194/acp-19-13267-2019>, 2019.
- 1037 Philip, S., Johnson, M. S., Baker, D. F., Basu, S., Tiwari, Y. K., Indira, N. K., Ramonet, M.,  
1038 and Poulter, B.: OCO-2 Satellite-Imposed Constraints on Terrestrial Biospheric CO<sub>2</sub> Fluxes  
1039 Over South Asia, *JGR Atmospheres*, 127, e2021JD035035,  
1040 <https://doi.org/10.1029/2021JD035035>, 2022.
- 1041 Potter, C. S., Randerson, J. T., Field, C. B., Matson, P. A., Vitousek, P. M., Mooney, H. A.,  
1042 and Klooster, S. A.: Terrestrial ecosystem production: A process model based on global  
1043 satellite and surface data, *Global Biogeochemical Cycles*, 7, 811–841,  
1044 <https://doi.org/10.1029/93GB02725>, 1993.
- 1045 Randel, W. J. and Park, M.: Deep convective influence on the Asian summer monsoon  
1046 anticyclone and associated tracer variability observed with Atmospheric Infrared Sounder  
1047 (AIRS), *Journal of Geophysical Research: Atmospheres*, 111,  
1048 <https://doi.org/10.1029/2005JD006490>, 2006.
- 1049 Randerson, J. T., Thompson, M. V., Conway, T. J., Fung, I. Y., and Field, C. B.: The  
1050 contribution of terrestrial sources and sinks to trends in the seasonal cycle of atmospheric  
1051 carbon dioxide, *Global Biogeochemical Cycles*, 11, 535–560,  
1052 <https://doi.org/10.1029/97GB02268>, 1997.

- 1053 Rathore, J., Ganguly, D., Singh, V., Gupta, M., Vazhathara, V. J., Biswal, A., Kunchala, R.  
1054 K., Patra, P. K., Sahu, L. K., Gani, S., and Dey, S.: Characteristics of Haze Pollution Events  
1055 During Biomass Burning Period at an Upwind Site of Delhi, *JGR Atmospheres*, 130,  
1056 e2024JD042347, <https://doi.org/10.1029/2024JD042347>, 2025.
- 1057 Rayner, P. J., Law, R. M., Allison, C. E., Francey, R. J., Trudinger, C. M., and Pickett-Heaps,  
1058 C.: Interannual variability of the global carbon cycle (1992–2005) inferred by inversion of  
1059 atmospheric CO<sub>2</sub> and  $\delta^{13}\text{C}$  measurements, *Global Biogeochemical Cycles*, 22,  
1060 <https://doi.org/10.1029/2007GB003068>, 2008.
- 1061 Reid, K. H. and Steyn, D. G.: Diurnal variations of boundary-layer carbon dioxide in a  
1062 coastal city—Observations and comparison with model results, *Atmospheric Environment*,  
1063 31, 3101–3114, [https://doi.org/10.1016/S1352-2310\(97\)00050-2](https://doi.org/10.1016/S1352-2310(97)00050-2), 1997.
- 1064 Russo, R. S., Talbot, R. W., Dibb, J. E., Scheuer, E., Seid, G., Jordan, C. E., Fuelberg, H. E.,  
1065 Sachse, G. W., Avery, M. A., Vay, S. A., Blake, D. R., Blake, N. J., Atlas, E., Fried, A.,  
1066 Sandholm, S. T., Tan, D., Singh, H. B., Snow, J., and Heikes, B. G.: Chemical composition  
1067 of Asian continental outflow over the western Pacific: Results from Transport and Chemical  
1068 Evolution over the Pacific (TRACE-P), *Journal of Geophysical Research: Atmospheres*, 108,  
1069 <https://doi.org/10.1029/2002JD003184>, 2003.
- 1070 Sawa, Y., Matsueda, H., Makino, Y., Inoue, H. Y., Murayama, S., Hirota, M., Tsutsumi, Y.,  
1071 Zaizen, Y., Ikegami, M., and Okada, K.: Aircraft Observation of CO<sub>2</sub>, CO<sub>2</sub> O<sub>3</sub> and H<sub>2</sub> over  
1072 the North Pacific during the PACE-7 Campaign, *Tellus B: Chemical and Physical*  
1073 *Meteorology*, 56, 2, <https://doi.org/10.3402/tellusb.v56i1.16402>, 2004.
- 1074 Schaaf, C. and Wang, Z.: MODIS/Terra+Aqua BRDF/Albedo Nadir BRDF-Adjusted Ref  
1075 Band6 Daily L3 Global 30ArcSec CMG V061,  
1076 <https://doi.org/10.5067/MODIS/MCD43D67.061>, 2021.
- 1077 Schaaf, C. B., Gao, F., Strahler, A. H., Lucht, W., Li, X., Tsang, T., Strugnell, N. C., Zhang,  
1078 X., Jin, Y., Muller, J.-P., Lewis, P., Barnsley, M., Hobson, P., Disney, M., Roberts, G.,  
1079 Dunderdale, M., Doll, C., d’Entremont, R. P., Hu, B., Liang, S., Privette, J. L., and Roy, D.:  
1080 First operational BRDF, albedo nadir reflectance products from MODIS, *Remote Sensing of*  
1081 *Environment*, 83, 135–148, [https://doi.org/10.1016/S0034-4257\(02\)00091-3](https://doi.org/10.1016/S0034-4257(02)00091-3), 2002.
- 1082 Schuck, T. J., Ishijima, K., Patra, P. K., Baker, A. K., Machida, T., Matsueda, H., Sawa, Y.,  
1083 Umezawa, T., Brenninkmeijer, C. a. M., and Lelieveld, J.: Distribution of methane in the  
1084 tropical upper troposphere measured by CARIBIC and CONTRAIL aircraft, *Journal of*  
1085 *Geophysical Research: Atmospheres*, 117, <https://doi.org/10.1029/2012JD018199>, 2012.
- 1086 Schuldt, K. N., Mund, J., Aalto, T., Abshire, J. B., Aikin, K., Allen, G., Andrade, M., Arlyn  
1087 Andrews, Apadula, F., Arnold, S., Baier, B., Bakwin, P., Bani, L., Bartyzel, J., Bentz, G.,  
1088 Bergamaschi, P., Beyersdorf, A., Biermann, T., Biraud, S. C., Pierre-Eric Blanc, Boenisch,  
1089 H., Bowling, D., Brailsford, G., Brand, W. A., Brunner, D., Bui, T. P. V., Van Den Bulk, P.,  
1090 Benoit Burban, Francescopiero Calzolari, Chang, C. S., Chen, G., Huilin Chen, Lukasz  
1091 Chmura, St. Clair, J. M., Clark, S., Sites Climadat, Coletta, J. D., Colomb, A., Commane, R.,  
1092 Condori, L., Conen, F., Conil, S., Couret, C., Cristofanelli, P., Cuevas, E., Curcoll, R., Daube,  
1093 B., Davis, K. J., Dean-Day, J. M., Delmotte, M., Dickerson, R., DiGangi, E., DiGangi, J. P.,  
1094 Van Dinter, D., Elsasser, M., Emmenegger, L., Shuangxi Fang, Forster, G., France, J.,  
1095 Frumau, A., Fuente-Lastra, M., Galkowski, M., Gatti, L. V., Gehrlein, T., Gerbig, C.,

- 1096 Francois Gheusi, Gloor, E., Goto, D., Griffis, T., Hammer, S., Hanisco, T. F., Hanson, C.,  
 1097 Haszpra, L., Hatakka, J., Heimann, M., Heliasz, M., Heltai, D., Henne, S., Hensen, A.,  
 1098 Hermans, C., Hermansen, O., Hintsa, E., Hoheisel, A., Holst, J., Di Iorio, T., Iraci, L. T.,  
 1099 Ivakhov, V., Jaffe, D. A., Jordan, A., Joubert, W., Kang, H.-Y., Karion, A., Kawa, S. R.,  
 1100 Kazan, V., Keeling, R. F., Keronen, P., Jooil Kim, Klausen, J., Kneuer, T., et al.: Multi-  
 1101 laboratory compilation of atmospheric carbon dioxide data for the period 1957-2023;  
 1102 *obspack\_co2\_1\_GLOBALVIEWplus\_v10.1\_2024-11-13*,  
 1103 <https://doi.org/10.25925/20241101>, 2024.
- 1104 Sharma, N., Dadhwal, V. K., Kant, Y., Mahesh, P., Mallikarjun, K., Gadavi, H., Sharma, A.,  
 1105 and Ali, M. M.: Atmospheric CO<sub>2</sub> Variations in Two Contrasting Environmental Sites Over  
 1106 India, *Air, Soil and Water Research*, 7, ASWR.S13987,  
 1107 <https://doi.org/10.4137/ASWR.S13987>, 2014.
- 1108 Sreenivas, G., Mahesh, P., Subin, J., Kanchana, A. L., Rao, P. V. N., and Dadhwal, V. K.:  
 1109 Influence of Meteorology and interrelationship with greenhouse gases  
 1110 (CO<sub>2</sub> and CH<sub>4</sub>) at a suburban site of India,  
 1111 *Atmos. Chem. Phys.*, 16, 3953–3967, <https://doi.org/10.5194/acp-16-3953-2016>, 2016.
- 1112 Sreenivas, G., P., M., Mahalakshmi, D. V., Kanchana, A. L., Chandra, N., Patra, P. K., Raja,  
 1113 P., Sesha Sai, M. V. R., Sripada, S., Rao, P. V. N., and Dadhwal, V. K.: Seasonal and annual  
 1114 variations of CO<sub>2</sub> and CH<sub>4</sub> at Shadnagar, a semi-urban site, *Science of The Total  
 1115 Environment*, 819, 153114, <https://doi.org/10.1016/j.scitotenv.2022.153114>, 2022.
- 1116 Srivastava, P., Bennett, M. W., Bedrosian, G., Rosenberg, R., Solish, B., and Basilio, R. R.:  
 1117 Establishing Launch Readiness of NASA ISS Instrument OCO-3, in: *IGARSS 2020 - 2020  
 1118 IEEE International Geoscience and Remote Sensing Symposium, IGARSS 2020 - 2020 IEEE  
 1119 International Geoscience and Remote Sensing Symposium, Waikoloa, HI, USA, 6101–6104*,  
 1120 <https://doi.org/10.1109/IGARSS39084.2020.9323631>, 2020.
- 1121 Stocker, T.F., D. Qin, G.-K. Plattner, L.V. Alexander, S.K. Allen, N.L. Bindoff, F.-M. Bréon,  
 1122 J.A. Church, U. Cubasch, S. Emori, P. Forster, P. Friedlingstein, N. Gillett, J.M. Gregory,  
 1123 D.L. Hartmann, E. Jansen, B. Kirtman, R. Knutti, K. Krishna Kumar, P. Lemke, J. Marotzke,  
 1124 V. Masson-Delmotte, G.A. Meehl, I.I. Mokhov, S. Piao, V. Ramaswamy, D. Randall, M.  
 1125 Rhein, M. Rojas, C. Sabine, D. Shindell, L.D. Talley, D.G. Vaughan and S.-P. Xie, 2013:  
 1126 Technical Summary. In: *Climate Change 2013: The Physical Science Basis. Contribution of  
 1127 Working Group I to the Fifth Assessment Report of the Intergovernmental Panel on Climate  
 1128 Change* [Stocker, T.F., D. Qin, G.-K. Plattner, M. Tignor, S.K. Allen, J. Boschung, A.  
 1129 Nauels, Y. Xia, V. Bex and P.M. Midgley (eds.)]. Cambridge University Press, Cambridge,  
 1130 United Kingdom and New York, NY, USA
- 1131 Stull, R. B. (Ed.): *An Introduction to Boundary Layer Meteorology*, Springer Netherlands,  
 1132 Dordrecht, <https://doi.org/10.1007/978-94-009-3027-8>, 1988.
- 1133 Summa, D., Di Girolamo, P., Stelitano, D., and Cacciani, M.: Characterization of the  
 1134 planetary boundary layer height and structure by Raman lidar: comparison of different  
 1135 approaches, *Atmospheric Measurement Techniques*, 6, 3515–3525,  
 1136 <https://doi.org/10.5194/amt-6-3515-2013>, 2013.
- 1137 Sun, Y., Frankenberg, C., Jung, M., Joiner, J., Guanter, L., Köhler, P., and Magney, T.:  
 1138 Overview of Solar-Induced chlorophyll Fluorescence (SIF) from the Orbiting Carbon

- 1139 Observatory-2: Retrieval, cross-mission comparison, and global monitoring for GPP, Remote  
1140 Sensing of Environment, 209, 808–823, <https://doi.org/10.1016/j.rse.2018.02.016>, 2018.
- 1141 Thilakan, V., Pillai, D., Sukumaran, J., Gerbig, C., Hakkim, H., Sinha, V., Terao, Y., Naja,  
1142 M., and Deshpande, M. V.: Potential of using CO<sub>2</sub> observations over India in regional carbon  
1143 budget estimation by improving the modelling system, EGU sphere, 1–32,  
1144 <https://doi.org/10.5194/egusphere-2023-1582>, 2023.
- 1145 Tiwari, Y., Valsala, V., Vellore, R., and Kunchala, R.: Effectiveness of surface monitoring  
1146 stations in representing regional CO<sub>2</sub> emissions over India, Clim. Res., 56, 121–129,  
1147 <https://doi.org/10.3354/cr01149>, 2013.
- 1148 Tiwari, Y. K., Vellore, R. K., Ravi Kumar, K., Van Der Schoot, M., and Cho, C.-H.:  
1149 Influence of monsoons on atmospheric CO<sub>2</sub> spatial variability and ground-based monitoring  
1150 over India, Science of The Total Environment, 490, 570–578,  
1151 <https://doi.org/10.1016/j.scitotenv.2014.05.045>, 2014.
- 1152 Vazhathara, V. J., Kunchala, R. K., & Philip, S. (2026). Measurement report: Insights into the  
1153 high temporal variability of atmospheric carbon dioxide (CO<sub>2</sub>) at a suburban station in the  
1154 Indo-Gangetic Plain [Data set]. Zenodo. <https://doi.org/10.5281/zenodo.19628722>
- 1155 Vermote, E. and NOAA CDR Program: NOAA Climate Data Record (CDR) of AVHRR  
1156 Normalized Difference Vegetation Index (NDVI), Version 5,  
1157 <https://doi.org/10.7289/V5ZG6QH9>, 2018.
- 1158 Wada, A., Matsueda, H., Sawa, Y., Tsuboi, K., and Okubo, S.: Seasonal variation of  
1159 enhancement ratios of trace gases observed over 10 years in the western North Pacific,  
1160 Atmospheric Environment, 45, 2129–2137, <https://doi.org/10.1016/j.atmosenv.2011.01.043>,  
1161 2011.
- 1162 Wang, G., Huang, J., Guo, W., Zuo, J., Wang, J., Bi, J., Huang, Z., and Shi, J.: Observation  
1163 analysis of land-atmosphere interactions over the Loess Plateau of northwest China, Journal  
1164 of Geophysical Research: Atmospheres, 115, <https://doi.org/10.1029/2009JD013372>, 2010.
- 1165 Wang, Z., Schaaf, C. B., Sun, Q., Shuai, Y., and Román, M. O.: Capturing rapid land surface  
1166 dynamics with Collection V006 MODIS BRDF/NBAR/Albedo (MCD43) products, Remote  
1167 Sensing of Environment, 207, 50–64, <https://doi.org/10.1016/j.rse.2018.02.001>, 2018.
- 1168 Watanabe, S., Miura, H., Sekiguchi, M., Nagashima, T., Sudo, K., Emori, S., and Kawamiya,  
1169 M.: Development of an atmospheric general circulation model for integrated Earth system  
1170 modeling on the Earth Simulator, Earth Simulator, 9, 27–35, 2008.
- 1171 Wigley, T. M. L. (1983). The pre-industrial carbon dioxide level. *Climatic change*, 5(4), 315-  
1172 320.
- 1173 Worthy, D. E. J., Chan, E., Ishizawa, M., Chan, D., Poss, C., Dlugokencky, E. J., Maksyutov,  
1174 S., and Levin, I.: Decreasing anthropogenic methane emissions in Europe and Siberia inferred  
1175 from continuous carbon dioxide and methane observations at Alert, Canada, Journal of  
1176 Geophysical Research: Atmospheres, 114, <https://doi.org/10.1029/2008JD011239>, 2009.
- 1177 Xiao, Y., Jacob, D. J., Wang, J. S., Logan, J. A., Palmer, P. I., Suntharalingam, P., Yantosca,  
1178 R. M., Sachse, G. W., Blake, D. R., and Streets, D. G.: Constraints on Asian and European

- 1179 sources of methane from CH<sub>4</sub> -C<sub>2</sub> H<sub>6</sub> -CO correlations in Asian outflow, *J. Geophys. Res.*,  
1180 109, 2003JD004475, <https://doi.org/10.1029/2003JD004475>, 2004.
- 1181 Xiong, X., Houweling, S., Wei, J., Maddy, E., Sun, F., and Barnett, C.: Methane plume over  
1182 south Asia during the monsoon season: satellite observation and model simulation,  
1183 *Atmospheric Chemistry and Physics*, 9, 783–794, <https://doi.org/10.5194/acp-9-783-2009>,  
1184 2009.
- 1185 Yoro, K. O. and Daramola, M. O.: CO<sub>2</sub> emission sources, greenhouse gases, and the global  
1186 warming effect, in: *Advances in Carbon Capture*, Elsevier, 3–28,  
1187 <https://doi.org/10.1016/B978-0-12-819657-1.00001-3>, 2020.
- 1188 Yuan, Y., Ries, L., Petermeier, H., Steinbacher, M., Gómez-Peláez, A. J., Leuenberger, M.  
1189 C., Schumacher, M., Trickl, T., Couret, C., Meinhardt, F., and Menzel, A.: Adaptive selection  
1190 of diurnal minimum variation: a statistical strategy to obtain representative atmospheric CO<sub>2</sub>  
1191 data and its application to European elevated mountain stations, *Atmospheric Measurement*  
1192 *Techniques*, 11, 1501–1514, <https://doi.org/10.5194/amt-11-1501-2018>, 2018.
- 1193 Zhang, H. F., Chen, B. Z., van der Laan-Luijk, I. T., Machida, T., Matsueda, H., Sawa, Y.,  
1194 Fukuyama, Y., Langenfelds, R., van der Schoot, M., Xu, G., Yan, J. W., Cheng, M. L., Zhou,  
1195 L. X., Tans, P. P., and Peters, W.: Estimating Asian terrestrial carbon fluxes from  
1196 CONTRAIL aircraft and surface CO<sub>2</sub> observations for the period 2006–2010,  
1197 *Atmospheric Chemistry and Physics*, 14, 5807–5824, [https://doi.org/10.5194/acp-14-5807-](https://doi.org/10.5194/acp-14-5807-2014)  
1198 2014, 2014.
- 1199 Zhang, X., Nakazawa, T., Ishizawa, M., Aoki, S., Nakaoka, S.-I., Sugawara, S., Maksyutov,  
1200 S., Saeki, T., and Hayasaka, T.: Temporal variations of atmospheric carbon dioxide in the  
1201 southernmost part of Japan, *Tellus B: Chemical and Physical Meteorology*, 59, 654–663,  
1202 <https://doi.org/10.1111/j.1600-0889.2007.00288.x>, 2007.
- 1203